MULTIFRACTAL CORRELATION USING WAVELET TRANSFORM MODULUS MAXIMA

BY

ASIF HASAN SHARIF

B. SC (HONS) UNIVERSITY OF TORONTO, 2003

A THESIS

PRESENTED TO RYERSON UNIVERSITY

IN PARTIAL FULFILLMENT OF THE
REQUIREMENTS FOR THE DEGREE OF
MASTER OF APPLIED SCIENCE
IN THE PROGRAM OF
MECHANICAL ENGINEERING

TORONTO, ONTARIO, CANADA, 2006

Author's Declararation

I hereby declare that I am the sole author of this thesis.

I authorize Ryerson University to lend this thesis or dissertation to other institutions or individuals for the purpose of scholarly research.

Signature ___

I further authorize Ryerson University to reproduce this thesis or dissertation by photocopying or by other means, in total or in part, at the request of other institutions or individuals for the purpose of scholarly research.

Signature ___

Abstract

MULTIFRACTAL CORRELATION USING WAVELET TRANSFORM MODULUS MAXIMA

Asif Hasan Sharif
Master of Applied Science
Graduate Program in Mechanical Engineering
Ryerson University
2006

The wavelet transform modulus maxima method (WTMM) for a single time series is generalized to multiple time series. The new method, which is called the joint WTMM analysis in this work, allows analyses of multifractal correlation between simultaneously measured data. Dependent, partly dependent and independent binomial cascades are used to test the joint WTMM formulism and the degree of correlation assessed qualitatively is found to agree well with the theoretical predictions. Finally, the technique is applied to simultaneously measured surface scalp potential and heart rate data taken from two healthy human subjects. Via this new method, it is shown that there is multifractal correlation between the fractal dynamics in the cortex and the autonomic regulation of the heart rate.

Acknowledgement

I am deeply indebted to my supervisor Dr. Bill Lin for his continuous support, guidance and encouragement throughout the Masters Program. I had many stimulating discussions with Dr. Lin that taught me valuable research skills and gave me the confidence to approach and solve complex problems. He spent many hours proofreading my thesis that he should have spent with his son Arthur. This thesis would not have been possible without him.

I also thank Dr. Hon Kwan (Department of Physiology, University of Toronto), who was my undergraduate supervisor, and the first person to introduce me to the world of fractals. He has always been a source of guidance and inspiration.

I thank my parents Mohammed and Rahena Tayab for their unconditional love and unwavering support in everything that I have done. They have always encouraged me to follow my dreams and given me the confidence and opportunity to do so. I thank my brother Adeeb Sharif for tolerating and accompanying me on all my crazy adventures. His perennial smile has always reassured me during difficult times.

Among my friends, I thank Jean-Jacques Boileau-Bekuit for all his help and support during my coursework and thesis, Stephanie Akers for assisting me with the mathematics and providing consistent encouragement, John Zamiska and Ahmed El Saadany for proofreading and support.

Table of Contents

List of Figures

List of Appendices

Nomenclature

D_B	box-counting dimension
$N(\varepsilon)$	number of line, plane or volume elements of size ε
$=_p$	equal in probability
$P_n(t)$	nth order polynomial
$\psi(t)$	analyzing wavelet
n_ψ	Order of polynomial that a wavelet ψ is orthogonal to
a	scale
$W[x](t,a)$	wavelet transform coefficient at time t and scale a
α	Holder exponent
$Z(\cdot)$	partition function
$P(x,y)$	probability of x given y
$\rho(x)$	probability distribution function of x
$\psi_{3G}(t)$	third derivative of the Gaussian analyzing wavelet
q	Moment
$\mathbf{q}$	(q_1, q_2)
$f(\alpha)$	Hausdorff dimension of the support α
α_0	α at which $f(\alpha)$ is a maximum
$\alpha_{\min}$	minimum α
$\alpha_{\max}$	maximum α
$B_H(t)$	fractional Brownian motion
$l(\cdot)$	wavelet transform maxima line
$L(a)$	set of all maxima lines at scale a
m_1, m_2	weight factors

$t(\bullet)$	location of wavelet transform maxima line
$\left\|\overline{W}_{k,j}\right\|$	supremum of $\left\|W[x_k](t,a')\right\|, a' \le a$ along the maximum line l_{kj}
$m,\ m'$	index of maxima line at scale a
$A_1, A_2,\ F$	canonical ensemble of partition function
$f(\alpha_1,\alpha_2)$	Hausdorff dimension of the support $\{(t,t'),\alpha_1,\alpha_2\}$
$\Gamma,\ M$	random variable between 0 and 1
γ	degree of correlation
$r(t)$	time interval between successive R waves
$E(t)$	raw EEG
$E_R(t)$	RRi aggregated EEG

CHAPTER 1 Introduction

Many physical systems exhibit data fluctuation that is neither completely random nor regular. In between, the 'object' now known as *fractal* was discovered to fit the characteristics of data fluctuation in almost all natural and artificial systems, ranging from the structure of the universe [1] to equity pricing [2], internet traffic [3] and DNA sequences [4].

Fractal objects are best described by the notion of self-similarity [5]. In terms of data fluctuation in physical systems, fractal is interpreted as the property of the (probability) measure [5, 6]. It is thus not too surprising that the machinery developed applies equally well to functions. Indeed, armed with the powerful tool of the wavelet, Hwang and Mallat [7], Bacry et. al. [8] and Ivanov et al. [9] have successfully characterized the fractality of functions. One important outcome of these advancements is the discovery of the highly non-uniform structure known as multifractal: an interwoven set of fractal objects. It is now accepted that most natural and artificial systems exhibit the multifractal property [7,8,9].

Multifractal objects have traditionally been studied using the so-called wavelet transform modulus maxima (WTMM) method. It is aimed at extracting the singularity spectrum that characterizes the distribution of the size of the degree of fluctuation. However, this method has only been developed for a single time series. The goal of this thesis is to extend the application of the WTMM method from the single time series case to the multiple time series case. The immediate advantage of a WTMM formulism for multiple time series is the opportunity to extract multifractal correlation from simultaneously measured signals, a generalization of the classical linear correlation analysis.

One of the main applications of multifractal correlation analysis is to characterize fluctuation patterns in biological systems. In particular, this allows one to analyze the 'connection' of fractal fluctuations that are known to exist in many physiological data taken from humans, such as the heart rate and brain wave fluctuation. In this work, the fractal fluctuations between the beat-to-beat heart rate and the surface scalp potential are studied. It was shown that such a correlation

does exist. It thus provides, the evidence of a 'fractal link' to the so-called heart rate variability problem in the higher centers of the brain.

In the next section, the notion of fractal is introduced in more specific terms. The fractal nature of heart rate variability and brain wave are reviewed in section 1.1 and the summary of the thesis is given in section 1.2.

1.1 Fractals

In connection to the idea of fractal, the mind typically conjures up images of static objects such as trees, a picture of the sky on a cloudy day or a flower. While this is true, one should be aware that the view does not reflect the evolution or generation of the structure of the fractal object. Furthermore, for complex dynamics of natural and artificial systems, the setting of such a geometrical framework is normally not possible. More commonly available is only the measured data. Therefore, it is necessary to extend the view of a geometric fractal to a probabilistic view of a fractal applied to signal fluctuation. Although the basis of such an extension is still covered in the realm of self-similarity, it is best described using the general notion of scale invariance symmetry. In this section, the construction and measure of geometrical fractal objects are first introduced using the basic example of a Cantor set. Its extension, based on the idea of scale invariance, follows to describe the fractal fluctuation of signals.

1.1.1 Construction and Measurement of Geometrical Fractal Objects

The Cantor set was proposed by the German mathematician G. Cantor in 1883 [10]. It is a classical example of a fractal and is often used to illustrate the properties of fractals. Its construction is quite simple and is outlined below.

Suppose that there is a unit interval $[0,1]$ at stage 0. At stage 1, the middle 1/3 of this line is removed. There are now two pieces of the interval left in stage 1: $[0,1/3]$ and $[2/3,1]$. At stage 2, the middle 1/3 of each of these two remaining intervals are again removed. Fig. 1 illustrates the construction.

Figure 1 Construction of the Cantor set in stages

If the intervals $[0,1/3]$ and $[2/3,1]$ in stage 1 are multiplied by 1/3, we get $[0,1/9]$ and $[2/9,1/3]$, which are the two intervals starting from the left at stage 2. If the intervals $[0,1/3]$ and $[2/3,1]$ in stage 1 are multiplied by 1/3, and translated by 2/3 we get $[2/3,7/9]$ and $[8/9,1]$, which are the two intervals starting from the right at stage 2. It is thus possible to create stage 2 of the Cantor set by a sequence of magnification and translation of stage 1. This captures exactly the mechanism of building the Cantor set in particular and other fractal objects in general. It also implies that the objects constructed from one stage to the next are only different in scale and location. This is the characteristic of scale invariance and is a fundamental feature of all fractal objects.

As this process continues *ad infinitum*, it is clear that the Cantor set becomes a point set. The size of the set has traditionally been the quantity of great interest. This can be measured from the notion of dimension. Dimension is related to how the target (fractal) object can be covered by a second (covering) object. Technically, it measures how the number of covering object scales with the size of the target object in the form of a power law. For example, the number N of line, plane and volume elements of size ε that are needed to cover any given line, plane and volume objects, respectively, scales as $N(\varepsilon) \sim \varepsilon^1$, $N(\varepsilon) \sim \varepsilon^2$ and $N(\varepsilon) \sim \varepsilon^3$. This is because, from common sense, these are one, two and three dimensional objects. Specifically, this is described as

$$D_B = \lim_{\varepsilon \to 0} \frac{\log N(\varepsilon)}{\log(1/\varepsilon)} \tag{1.1}$$

The subscript 'B' in the notation means 'box counting' and refers to the nature of the process. By the same idea, one can cover the Cantor set with small line segments of size $(1/3)^i$. It would then require $N(\varepsilon) = 2^i$ of such line segments to cover the Cantor set at each stage of the construction. Therefore, the (box-counting) dimension for the Cantor set is [10]

$$D_B = \lim_{i\to\infty} \frac{\log 2^i}{\log 3^i} \approx 0.6309 \tag{1.2}$$

Fractals in nature are more complex objects than the Cantor set in that (1.1) no longer holds uniformly over the whole fractal set. As a result, one must discuss the spatial dependence of (1.1). Intuitively, the fractal set may be considered as consisting of interwoven pieces of Cantor sets of different dimensions. Associated with such a 'dimension spectrum' is the 'degree of clustering' of the set. This is, in essence, the characterization of multifractal objects. The application of the multifractal concept in time series modeling will be discussed at length in Chapter 2. In the next section, a review of generalization of the geometrical fractal concept to time series analysis is given.

1.1.2 Fractal Analysis of Signal Fluctuation

Let $x(t)$ be a discrete-time, real-value process. This mimics most experimental situations, where the dynamics of the physical system of interest are measured with a fixed sampling time. The fluctuation is analyzed in the time domain based on the idea of scale-invariance symmetry. The process $x(t)$ is said to possess continuous scale invariance symmetry, if its probability distribution is preserved after the change of variables, $t \to \lambda t, x \to x/\mu$, where λ and $\mu(\lambda)$ are real numbers, i.e.,

$$x(t) =_p \frac{1}{\mu(\lambda)} x(\lambda t) \tag{1.3}$$

where $=_p$ means 'equal in probability.' There is also a discrete version of the scale invariance which can give rise to log-periodic oscillation of the fractal property [11].

Assume $x(t^*)=0$. Equation (1.3) implies $x(t)$ in time interval $[t^*, t^*+\Delta t]$ has a similar appearance as in $[t^*, t^*+\lambda\Delta t]$ after rescaling of amplitude by the factor $1/\mu$. Hence, the idea of analyzing fractal fluctuation is similar to the idea of self-similarity used in the study of geometrical fractal objects. If the probability distribution of $x(t)$ can be found, it is possible to characterize the strength of fluctuation as a function of time and estimate the dimension of the interval occupied by the specific strength of fluctuation. Therefore, the notions of strength of fluctuation and the dimension of the corresponding intervals, are the counterparts of clustering and dimension of geometrical multifractal objects. As is mostly the case, the probability function of experimental data is unknown and one relies on the estimate of moments to achieve the same goal. These abstract settings can be made precise with the specific tool used to characterize the relationship (1.3). They will be discussed in detail in the following chapters.

1.2 Summary of Thesis

This thesis is divided into five chapters. Chapter two first details the existing method of obtaining multifractal spectra using WTMM, and subsequently applies it to the binomial cascade and fractional Brownian motion. Chapter three constructs the joint multifractal spectra using WTMM, and then three sets of time-series are created: completely dependent, partly dependent and completely independent by modifying the binomial cascade. Next, the joint multifractal spectra of the time-series are compared. In chapter four, surface scalp potential and beat-to-beat heart rate are obtained from human subjects and are studied using the newly defined method. Chapter five summarizes the conclusions of the thesis and identifies possible areas of future research.

CHAPTER 2 Multifractal Spectra using Wavelet Transform

2.1 Multifractal Formalism

Random fluctuation in many natural and artificial systems can be quantified via the notion of singularity. Let $x(t)$ be the data of interest. Treated as a function, its singular property can be measured by the so-called local Hölder exponent. It is defined as the greatest exponent α such that, for some $\delta_0 > 0$, $C(t) > 0$ and an n^{th} order polynomial $P_n(t)$ with $n < \alpha$, the following inequality holds

$$\left|x(t+\delta) - P_n(t)\right| \le C|\delta|^{\alpha(t)} \tag{2.1}$$

$\forall \delta < \delta_0$. If $x(t)$ is n times continuously differentiable at t, $P_n(t)$ can be selected as the order n Taylor expansion of x at t and therefore, $\alpha < n$. This also means that the larger the exponent α, the more regular x is at t. It is also important to note that (2.1) is a point-wise definition. This allows the singular property to be studied as a function of scale. The natural tool to accomplish this is by the wavelet transform:

$$W[x](t,a) = \frac{1}{a}\int_{-\infty}^{\infty} \psi\left(\frac{t'-t}{a}\right) x(t')\,dt' \tag{2.2}$$

where $W[x](t,a)$ is the wavelet coefficient and $\psi(t)$ is the analyzing wavelet that is designed to be well localized at $t = 0$ [12]. On account of the need to delete the polynomial trend, analyzing wavelets that are orthogonal to polynomials are considered. This means that the wavelet satisfies $\int t^m \psi(t)dt = 0$ for some $0 < m < n_\psi$, where n_ψ is the order of the polynomial. The derivatives of the Gaussian function, known as the Gaussian wavelets, are used in this work to fulfill this condition.

For a well localized ψ at $t = 0$ that is orthogonal to all polynomials up to the order $n_\psi > \alpha(t)$, one can integrate both sides of (2.1) against $\psi((t'-t)/a)$ and find, as $a \to 0^+$,

$$W[x](t,a) \sim a^{\alpha(t)} \tag{2.3}$$

[8]. Thus, in principle, by choosing ψ with a large enough n_ψ, the entire set $\{\alpha\}$ can be obtained. Let the plane spanned by t and a be called the *time-scale plane*. Hwang and Mallat [7] identified

the geometrical object associated with (2.3) in the time-scale plane, namely, there exists a maxima line $\{(t,a)\}$ originating at t where (2.3) holds. Here, the maxima line is defined by the points in the time-scale plane where the wavelet modulus is a local maximum:

$$\{(t,a),|W[x](t',a)|<|W[x](t,a)|,t'\in[t-\varepsilon_1(t,a),t+\varepsilon_2(t,a)]\} \tag{2.4}$$

Using the maxima line to study the singular property of a function has been known as the method of wavelet transform modulus maxima (WTMM).

Based on WTMM, the deeper structure of $\{\alpha\}$ can be established by considering a statistical physics analogy of the partition function. The idea is to use $W[x]\sim a^{\alpha(t)}$ as a measure of the singularity of $x(t)$ in the time-scale plane. From the definition of the partition function in statistical mechanical systems, the partition function analogue of WTMM can be given by

$$Z(a,q)=\int|W[x](t,a)|^q\,dt, q\in\mathbb{R} \tag{2.5}$$

In this analogy, $|W[x]|$ may be compared to the exponential of the energy state and q to the inverse of temperature of the canonical ensemble, see [13]. Assuming the probability density function (PDF) $\rho(\alpha)$, the α distribution in scale a can be given by $\rho(\alpha)a^{-f(\alpha)}$, where $f(\alpha)$ is the Hausdorff dimension of the support $\{h(t)=\alpha\}$. Introducing (2.3) into (2.5), one can approximate the integral in small a as

$$Z(a,q)\sim a^{\tau(q)} \tag{2.6}$$

As a result, $\tau(q)$ and $f(\alpha)$ can be shown to be a Legendre transform pair (Appendix A) [14]:

$$\tau(q)=\min_{\alpha}(q\alpha-f(\alpha)) \tag{2.7}$$

Given $f(\alpha)$, the probability of finding an α interval in the real line $x(t)$ can also be found as a power law function of a:

$$P(\alpha,a)=\frac{\text{number of intervals with }\alpha}{\text{number of intervals of width }a}\sim a^{-f(\alpha)+1} \tag{2.8}$$

In the current literature, $f(\alpha)$ is known as the singularity spectrum of $x(t)$. Unfortunately, calculating (2.5) in practice can be problematic since it can diverge for negative q when

$W[x](t,a)=0$. To overcome this problem, Arneodo et al. pointed out the novel idea of scale-adaptive partitioning of the time-scale plane to estimate Z [4]:

$$Z(a;q)=\sum_{l\in L(a)}\left(\sup_{(t,a')\in l}|W[x](t,a')|^q\right) \tag{2.9}$$

where $L(a)$ denotes the set of all maxima lines at scale a. The adaptivity of the method derives from the sup norm in (2.9). Hence, the contribution to the scaling relation of the partition function comes from the supremum of the maxima line.

The Gaussian wavelet family used in this work is derived by taking derivatives of the Gaussian function $\psi_G = f(x)=e^{\frac{-t^2}{2}}$. All results are based on the third derivative unless otherwise specified.

$$\psi_{3G}(t)=\left(3t-t^3\right)e^{\frac{-t^2}{2}} \tag{2.10}$$

The singularity is studied based on the partition function (2.8), and $\tau(q)$ is estimated from the slope of the log-log plot of $Z(a;q)$ versus a. Finally, $f(\alpha)$ is found by taking the Legendre transform of $\tau(q)$.

2.2 Numerical Examples

Two examples are shown to illustrate the WTMM approach outlined above. The first is the binomial cascade with continuous division and redistribution of mass in the unit interval. The binomial cascade is known to exhibit fluctuation characterized by a range of Holder exponents. The second example is the so-called fractional Brownian motion which has a degenerate singularity spectrum characterized by a single Holder exponent.

2.2.1 Binomial Cascade

The binomial cascade is constructed iteratively according to the following steps. Consider an initial cascade value $\mu_0 = 1$ in the unit interval $I_0 = [0,1]$. The unit interval will go through n-divisions into smaller intervals by a factor of 2; e.g., $I_1 = \{[0,1/2], (1/2,1]\}$, $I_2 = \{[0,1/4], (1/4,1/2], (1/2, 3/4], (3/4, 1]\}$, ..., $I_n = \{[0,2^{-n}], (2^{-n},2^{-n+1}],..., ((2^n - 1)2^{-n},1]\}$. During each division, the cascade value is modified by multiplication of weight factors m_1, m_2 to the value of the previous interval. For example, the two intervals in I_1 [0,1/2] and (1/2, 1] will carry, respectively, m_1 and $m_2 = 1 - m_1$ portions of $\mu_0 = 1$ of the unit mass in [0,1]. Similarly, the 2^n intervals in I_n have the values m_1^n, $m_1^{n-1} m_2$, ..., m_2^n, following the order of appearance of the intervals in I_n. The name binomial cascade is thus evident as these cascade values are nothing but the binomial expansion of the powers of the sum of two variables m_1 and m_2.

Fig. 2 depicts the first three steps of the construction of a binomial cascade with $m_1 = 0.8$, and $m_2 = 0.2$.

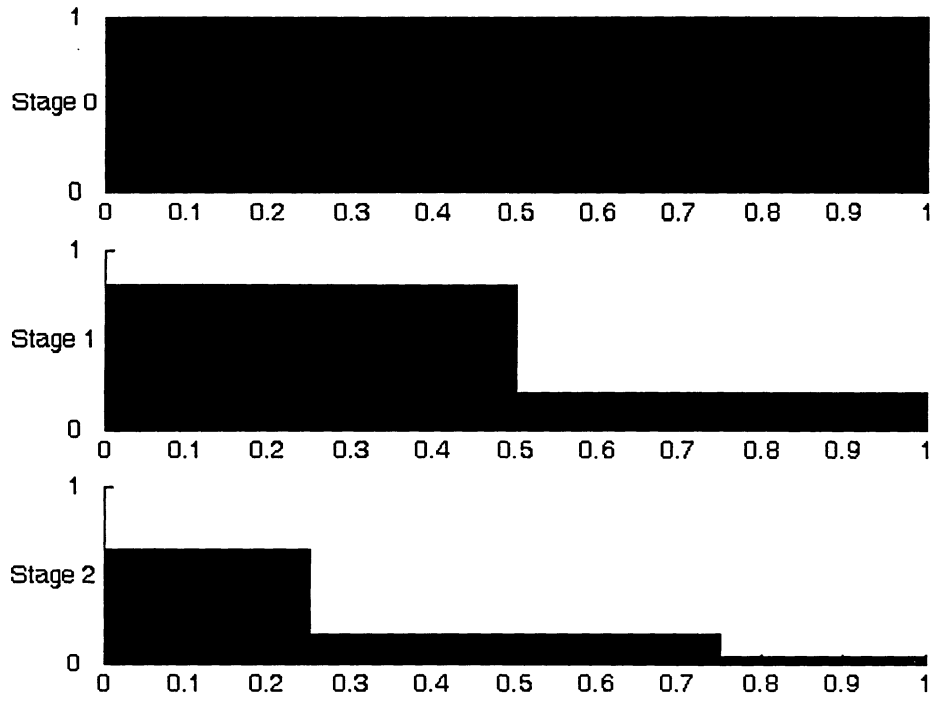

Figure 2 Construction of the binomial cascade

The partition function can be derived for the binomial cascade as [10]:

$$Z(2^{-k},q)=\left(m_1^q+m_2^q\right)^k \tag{2.11}$$

where k is the number of iterations. Using (2.6) and (2.7), one can find:

$$\tau(q)=-\log_2\left(m_1^q+m_2^q\right) \tag{2.12}$$

The Legendre transform of (2.12) gives α and $f(\alpha)$

$$\begin{aligned}\alpha &= \frac{m_1^q\log_2(m_1)+m_2^q\log_2(m_2)}{\left(m_1^q+m_2^q\right)}\\ f(\alpha) &= \frac{qm_1^q\log_2(m_1)+qm_2^q\log_2(m_2)-\log_2\left(m_1^q+m_2^q\right)m_1^q-\log_2\left(m_1^q+m_2^q\right)m_2^q}{\left(m_1^q+m_2^q\right)}\end{aligned} \tag{2.13}$$

Note that the maximum of $f(\alpha)$ is located at $q=0$ and the α value usually denoted as α_0 is given by:

$$\alpha_0=-\frac{1}{2}\log_2 m_1m_2=1.32 \tag{2.14}$$

For the binomial cascade, one can also find the maximum and minimum of α at $f(\alpha)=0$:

$$\alpha_{\min} = -\log_2 m_1 = 0.32$$
$$\alpha_{\max} = -\log_2 m_2 = 2.32 \qquad (2.15)$$

Fig. 3a shows the generated cascade. It was integrated before WTMM was applied (Fig. 3b). Poor statistics in large q_1, q_2, values are seen to cause difficulty in estimating the power law; thus, the range of q used in the partition function was limited from -4 to +4 with increments of 0.5. Fig. 4 shows the $\tau(q)$ curve of the binomial cascade. The characteristic concavity of the function is typical for a multifractal signal. Fig. 5 shows the comparison between numerically estimated $f(\alpha)$ and the analytical result (2.12). It is evident that they are in good agreement.

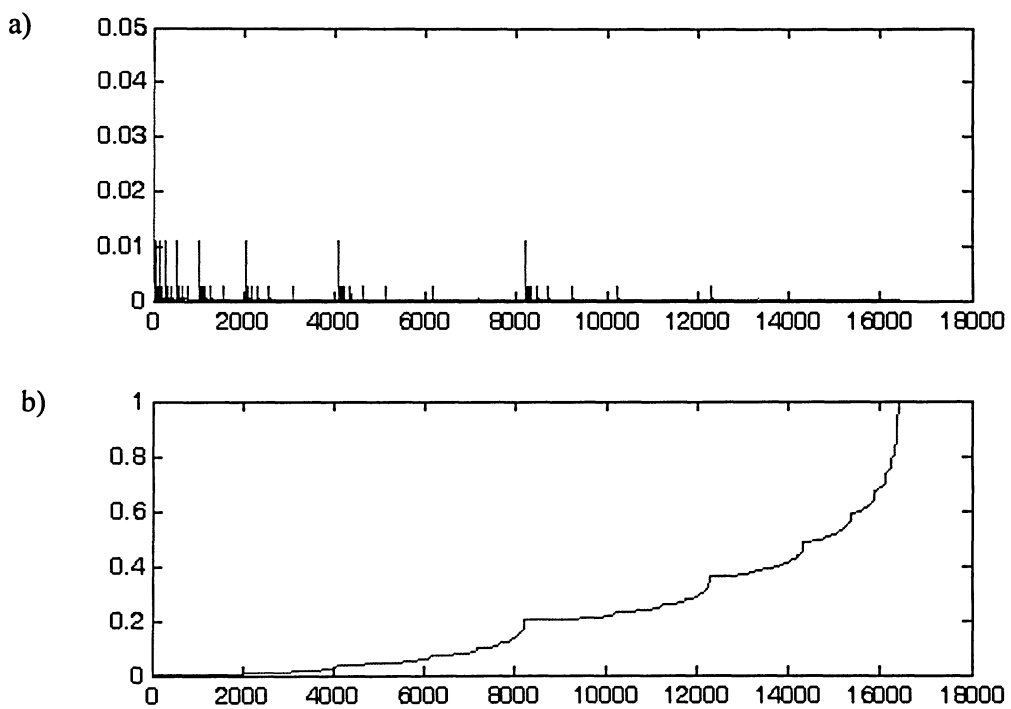

Figure 3 The binomial cascade a) The cascade after 16 iterations. b) The integrated binomial cascade.

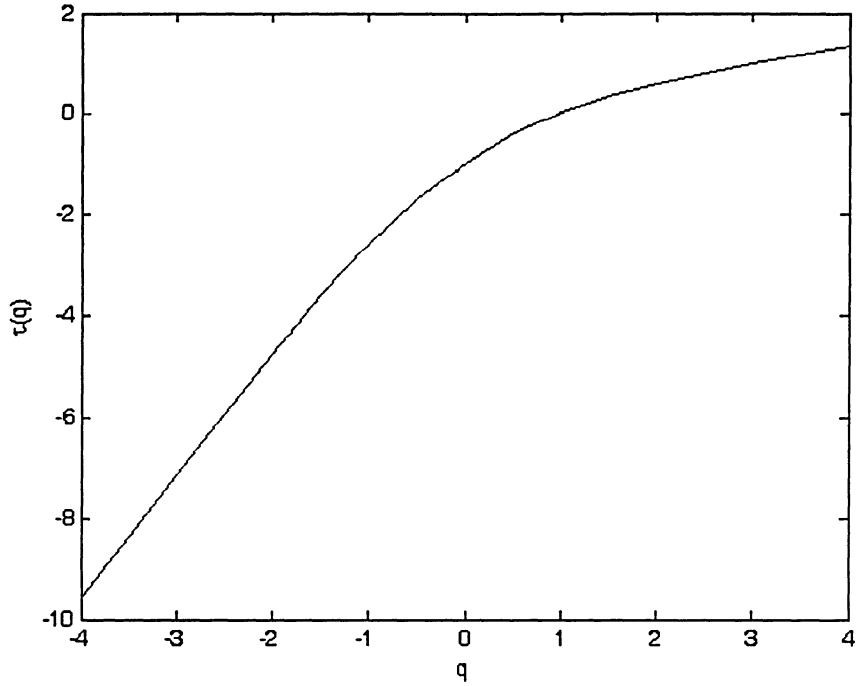

Figure 4 q vs $\tau(q)$ for the binomial cascade. The curve is clearly non-linear.

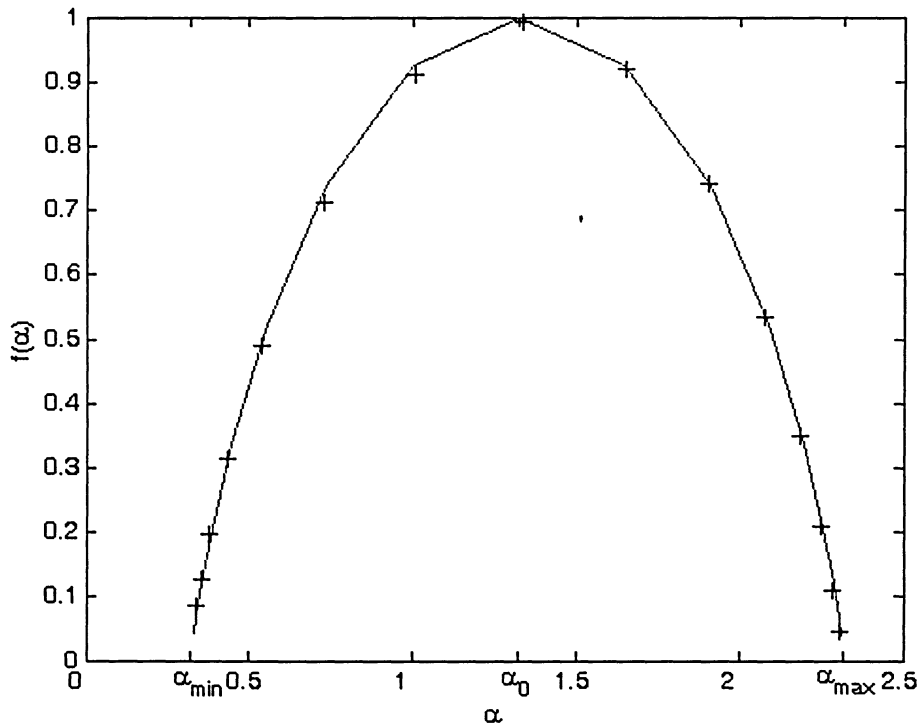

Figure 5 Numerical $f(\alpha)$ (crosses) and theoretical $f(\alpha)$ (solid line) for the binomial cascade. In this example, the first derivative of the Gaussian function was used.

2.2.2 Fractional Brownian Motion

Let $B_H(t)$ denote fractional Brownian Motion (fBm), where the subscript H is called the Hurst exponent of fBm. It is known for three distinct properties: (a) its increment is Gaussian distributed, (b) its increment is correlated and (c) it is self-similar in that $B_H(at) =_p |a|^H B_H(t)$, where $=_p$ means equal in probability. Due to its self-similarity, it can be shown almost surely that $B_H(t)$ is nowhere differentiable. Furthermore, fBm is 'mono-fractal' in that its singular spectrum is degenerate to a singleton $\alpha = H$, the Hurst exponent of fBM. The derivation of these important characteristics is beyond the scope of this thesis and interested readers are referred to the reference [15].

In the numerical experiment, $B_H(t)$ of 16384 points with Hurst exponent 0.3 and 0.8 were generated using the Levinson method [16]. Figs. 6a and 6b demonstrate the difference between the two cases. Fig. 6a is an example of anti-persistent motion, i.e., an upward 'spike' of the signal is likely to be followed by a downward 'spike' of the signal. Fig. 6b is an example of persistent motion which has a trend converse to the antipersistent case; i.e., an upward 'spike' of the signal is likely to be followed by an upward 'spike' and vice versa. The range q for the partition function was taken from -3 to +3 with an increment of 0.2 as evident from the τ curves of Figs 6c and 6d. In Fig 6e and 6f, the numerical α_0 for the curves are approximately 0.29 and 0.82 respectively and the dark vertical line represents the theoretical Hurst exponent of 0.3 and 0.8 respectively. Theoretically, the $f(\alpha)$ curves of Figs. 6e and 6f should be a point, but due to numerical approximations a small range is observed instead.

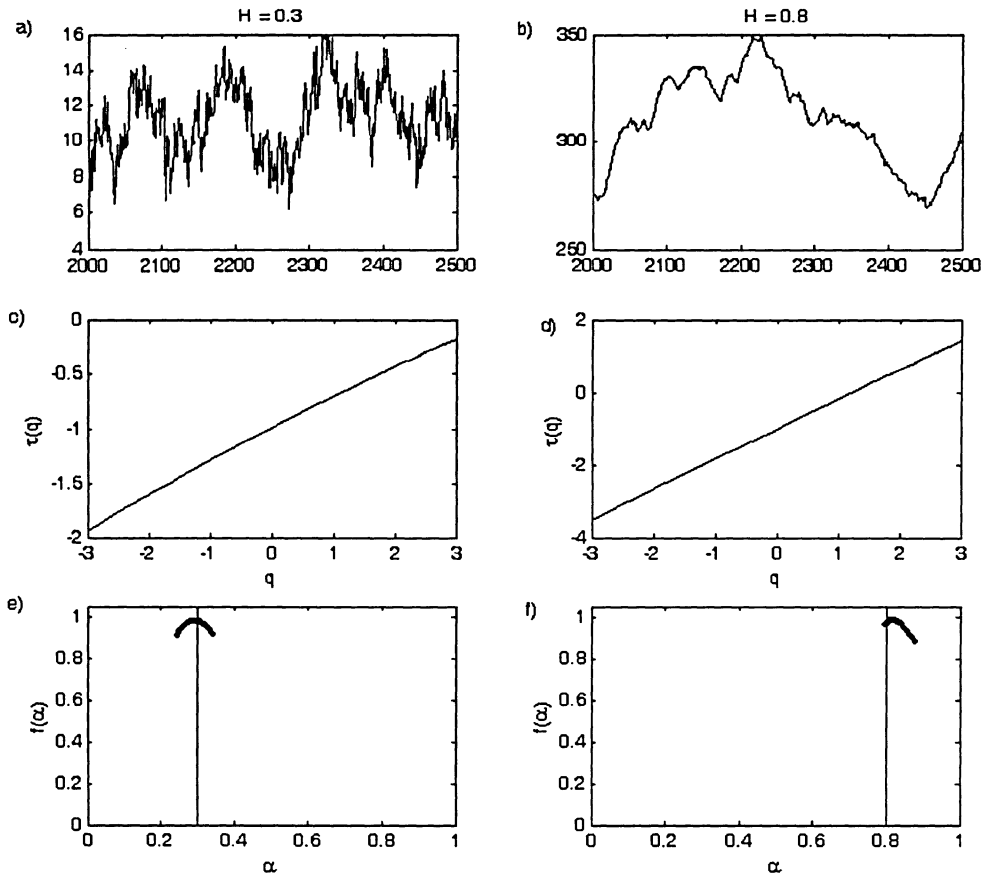

Figure 6 Analysis of Brownian Motion using WTMM a) and b) fractional Brownian motion with Hurst exponent 0.3 and 0.8 respectively. c) and d) τ curves of the respective fBm. e) and f) $f(\alpha)$ spectrum.

CHAPTER 3 Joint Multifractal Correlation using Wavelet Transform Modulus Maxima

For multiple signals measured simultaneously, the issue of multifractal correlation arises naturally. For example, multifractality is observed in both the velocity and temperature fields of hydrodynamic turbulence [17]. Since the laws of momentum and energy balance govern the dynamics of these field variables, multifractality between them are likely correlated. Indeed, Meneveau et al. [18] showed the existence of such multifractal correlation. The purpose of this chapter is to formulate the joint WTMM approach to tackle the multifractal correlation problem from simultaneously measured temporal signals. In what follows, the WTMM analysis discussed above will be referred to as the 1D WTMM analysis, and the joint WTMM approach introduced below as the 2D WTMM analysis.

3.1 Joint Multifractal Spectra using Wavelet Transform Modulus Maxima

In the joint multifractal analysis, consider simultaneous measurements of $x_1(t)$ and $x_2(t)$ from the same physical system. Assume individual sets of Holder exponents $\{\alpha_1\}$ and $\{\alpha_2\}$, respectively. Let $L_k(a) = \{l_{k,1}(a), \ldots, l_{k,N_k}(a)\}$ be the wavelet transform maxima lines of $x_k(t)$, $k = 1,2$, at scale a, where $N_k(a)$ denotes the number of maxima lines. Note that, in general, $N_1(a) \neq N_2(a)$. To extend the 1D WTMM analysis to the 2D case, these lines must be paired properly. In this work, it is assumed that, if the singularities of $x_1(t)$ and $x_2(t)$ are correlated, their respective maxima lines are also closed in the time-scale plane. Let the locations of any two maxima lines $l_{1,m}(a), l_{2,m'}(a)$ be $t_{1,m}(a)$ and $t_{2,m'}(a)$ respectively, where m and m' are integers. Their pairing is determined by the following condition

$$t_{1,m} = \min_{l=1..N_1(a)} \left| t_{1,l} - t_{2,m'} \right| \tag{3.1}$$

$$t_{2,m'} = \min_{l'=1..N_2(a)} \left| t_{1,m} - t_{2,l'} \right| \tag{3.2}$$

Given a, let the supremum of $|W[x_k](t,a')|, a' \le a$ along the maximum line $l_{kj} \in \mathcal{L}_k(a)$ be denoted as $|\overline{W}_{k,j}|$. Following the WTMM analysis described in Chapter 2, a joint partition function may be defined as:

$$Z(a;\mathbf{q}) = \sum_j |\overline{W}_{1,j}|^{q_1} |\overline{W}_{2,j}|^{q_2} \tag{3.3}$$

where $\mathbf{q} = (q_1, q_2)$.

However, there is a potential problem with this straightforward implementation. Specifically, when $q_1 = 0$ ($q_2 = 0$), (3.3) is contributed only by the WTMM of $x_1(t)$, $x_2(t)$ and should equal the partition function of the individual time series (see(2.8)). Since $N_1(a) \neq N_2(a)$ in general, (3.1) and (3.2) are not always satisfied and there will be maxima lines at scale a that are not paired. As a result, the individual partition function will not be recovered at $q_i = 0$, i = 1,2. In order to include these un-paired lines, phantom lines of $\overline{W}_{k,j}^{(p)} = 0, k = 1,2$, are introduced to pair with the lone $\overline{W}_{k,j}$. The effect is the recovery of individual partition function at $q_1 = 0, q_2 = 0$ as $0^0 = 1$ is adopted in the numerical computation. Fig. 7 is a visual illustration of this method. The x-axis represents the location of a coefficient on the maxima line. The dots at the bottom represent the location of a coefficient on one time-series $t_{1,m}(a)$, and the dots on the top represent the location of the other $t_{2,m'}(a)$. Insertions of zeroes are denoted by empty circles and the dashed line shows the pairing of the coefficients. Clearly, for $q_1, q_2 \neq 0$, the lone $\overline{W}_{k,j}$ has no contribution to the sum due to the pairing with $\overline{W}_{k,j}^{(p)} = 0$. Hereafter, the superscript (p) of $\overline{W}_{k,j}^{(p)} = 0$ will be dropped.

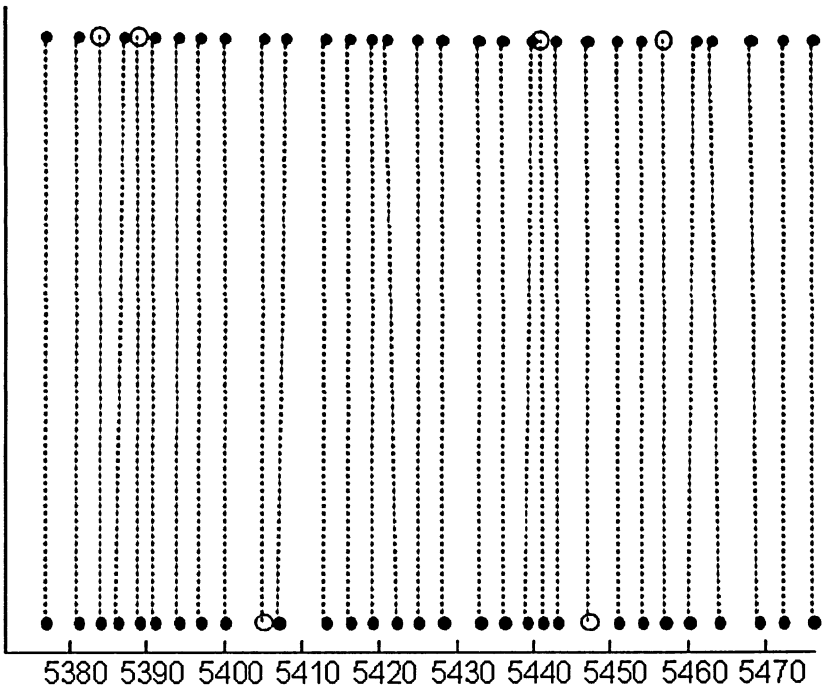

Figure 7 Pairing up of the WTMM coefficients.

Generalizing (3.3) in the 2D case reads

$$Z(a;\mathbf{q}) \sim a^{\tau(\mathbf{q})} \tag{3.4}$$

Substituting the results by Hwang and Mallat [7]

$$\left|\bar{W}_{k,j}\right| \sim a^{h_k}, k = 1,2 \tag{3.5}$$

into (3.3) yields

$$Z(a;\mathbf{q}) \sim \sum_j a^{q_1\alpha_1+q_2\alpha_2} \sim \iint d\alpha_1 d\alpha_2 P(\alpha_1,\alpha_2) a^{q_1\alpha_1+q_2\alpha_2-f(\alpha_1,\alpha_2)} \tag{3.6}$$

where $P(\alpha_1,\alpha_2)$ is the joint PDF of (α_1,α_2) and $f(\alpha_1,\alpha_2)$ is the Hausdorff dimension of the support $\{(t,t'),\alpha_1,\alpha_2\}$. By the same argument used in the 1-dimensional case, one has with (3.4):

$$\tau(\mathbf{q}) = \min_{\alpha_1,\alpha_2}\left(q_1\alpha_1 + q_2\alpha_2 - f(\alpha_1,\alpha_2)\right) \tag{3.7}$$

From the minima of (3.7) achieved at

$$q_1 = \frac{\partial f}{\partial \alpha_1}, \quad q_2 = \frac{\partial f}{\partial \alpha_2} \tag{3.8}$$

$\tau(\mathbf{q})$ and $f(\alpha_1,\alpha_2)$ are seen to form the double Legendre transform pair:

$$\begin{aligned}\alpha_1 &= \frac{\partial\tau(\mathbf{q})}{\partial q_1}\\ \alpha_2 &= \frac{\partial\tau(\mathbf{q})}{\partial q_2}\\ f(q_1,q_2) &= \alpha(\mathbf{q})q_1+\alpha(\mathbf{q})q_2-\tau(q_1,q_2)\end{aligned} \tag{3.9}$$

In practice, the success of the above approach relies on performing the Legendre transform (3.7) using $\tau(\mathbf{q})$ estimated from (3.4). However, there are known factors, such as lacunarity [19], that introduce an oscillatory, scale dependent, prefactor in (3.4). This results in a poor estimate of $\tau(\mathbf{q})$. An alternative approach that is equivalent to the canonical ensemble in statistical physics can be used to minimize such "effects" in the 1-dimensional case [20]. In 2-dimensions, it is straightforward to generalize to define a joint canonical measure:

$$v(j,a;\mathbf{q}) = \frac{|W_{1,j}|^{q_1}|W_{2,j}|^{q_2}}{Z(a;\mathbf{q})} \tag{3.10}$$

Using v, consider the following averages [18]

$$A_1(a;\mathbf{q}) = \sum_j v(j,a;\mathbf{q})\log\left(|\overline{W}_{1,j}|\right) \tag{3.11}$$

$$A_2(a;\mathbf{q}) = \sum_j v(j,a;\mathbf{q})\log\left(|\overline{W}_{2,j}|\right) \tag{3.12}$$

and

$$F(a,\mathbf{q}) = \sum_j v(j,a;\mathbf{q})\log\left(v(j,a;\mathbf{q})\right). \tag{3.13}$$

With straightforward manipulations, (Appendix C), the following scaling laws can be established

$$A_k(a;\mathbf{q}) \sim \alpha_k(\mathbf{q})\log(a) \tag{3.14}$$

for $k = 1, 2$, and

$$F(a;\mathbf{q}) \sim f(q_1,q_2)\log(a). \tag{3.15}$$

3.2.1 Validation

In (2.8), it was shown that the probability of finding an interval with Hölder exponent scales as $\sim a^{-f(\alpha)+1}$. By the same reasoning, a similar result can be obtained in the joint case:

$$P(a,\alpha_1,\alpha_2) \sim a^{-f(\alpha_1,\alpha_2)+1} \tag{3.16}$$

Equation (3.16) provides a way to construct a marginal relationship between $f(\alpha_1,\alpha_2)$ and $f(\alpha_1), f(\alpha_2)$. Specifically using the marginal probability,

$$P(\alpha_1) = \int P(\alpha_1,\alpha_2) d\alpha_2 \tag{3.17}$$

and substituting (2.8) and (3.16) into the above, one has

$$f(\alpha_1) = \max_{\alpha_2} f(\alpha_1,\alpha_2) \tag{3.18}$$

by approximating (3.17) by the maximum of the integrand in small a. Similarly,

$$f(\alpha_2) = \max_{\alpha_1} f(\alpha_1,\alpha_2) \tag{3.19}$$

3.3 Numerical Examples

To demonstrate the proposed joint WTMM analysis, two random binomial cascades are generated with built-in correlation in their weights. The idea is, at any level of the construction (see section 2.2.1), the weights assigned to the offspring intervals of one cascade determine, depending on the degree of correlation, the weights assigned for the second cascade.

Specifically, assume the weight factors m_1, m_2 and m_1', m_2' are used in the construction of cascades $x_1(t)$ and $x_2(t)$, respectively. Let $I_{k,L}$, $I_{k,R}$ be the newly created left and right intervals $k =$ 1, 2. Let M and Γ be uniformly distributed random variables in [0,1]. To build the random cascade, assume probabilities M, $1 - M$, respectively, of assigning weights m_1, m_2 to $I_{1,L}$, $I_{1,R}$ of $x_1(t)$. The weights assigned to $I_{2,L}$ and $I_{2,R}$ for $x_2(t)$ are related to those for $x_1(t)$ according to the draw of Γ in [0,1]: for a fixed $\gamma \in$ [0,1],

- m_1' is assigned to $I_{2,L}$ and m_2' to $I_{2,R}$, if $\Gamma < \gamma$,
- m_1' is assigned to $I_{2,L}$ with probability M_1 and m_2' to $I_{2,L}$ with probability $1 - M_1$, if $\Gamma \geq \gamma$,

It is clear, depending on the value of γ, the weights assigned to x_1, x_2 range from being entirely dependent ($\gamma = 1$) to entirely independent x_1, x_2 ($\gamma = 0$). For $0 < \gamma < 1$, the cascades are partially dependent on each other.

Shown in Fig. 8 are examples of the cascades generated using $(m_1, m_2) = (0.2, 0.8)$, $(m_1', m_2') = (0.4, 0.6)$ and different γ values. It is evident that the larger the difference of the weight factors, the more intermittent the fluctuation becomes. While different weight factors are seen to create particular appearances of the cascade, the different fluctuation patterns becomes visually evident as γ approaches 1 (totally independent).

The correlation of the cascades x_1, x_2 can be derived explicitly. Since the weights between cascade steps are generated independently, one has:

$$Z(a;q_1,q_2) = \sum |\overline{W}_{1,j}|^{q_1} |\overline{W}_{1,j}|^{q_2} \sim a^{-1} \left\langle |\overline{W}_{1,j}|^{q_1} |\overline{W}_{2,j}|^{q_2} \right\rangle \sim a^{-1} \left\langle \prod_{i=1}^{J} M_1^{q_1} M_2^{q_2} \right\rangle \quad (3.20)$$
$$\sim a^{-1} \left\langle M_1^{q_1} M_2^{q_2} \right\rangle^J$$

where M_1 denotes the weight factor (m_1 or m_2) of x_1 and M_2 denotes the weight factor (m_1 ' or m_2 ') of x_2. With γ–dependent, $(1-\gamma)$–independent weight factor assignment, one has

$$\left\langle M_1^{q_1} M_2^{q_2} \right\rangle = \gamma \frac{(m_1^{q_1} m'^{q_2}_1 + m_2^{q_1} m'^{q_2}_2)}{2} + (1-\gamma) \frac{(m_1^{q_1} m'^{q_2}_2 + m_2^{q_1} m'^{q_2}_1 + m_1^{q_1} m'^{q_2}_1 + m_2^{q_1} m'^{q_2}_2)}{4} \quad (3.21)$$

In (3.21), the two terms multiplied by the γ are the only weight factor combinations in the fully dependent case, and the remaining four terms are the combinations in fully independent case. Substituting (3.21) into (3.20) and factor out the power law exponent of $a = 2^{-J}$ yields

$$\tau(q_1,q_2) = \log_2 \left(\gamma (m_1^{q_1} m'^{q_2}_1 + m_2^{q_1} m'^{q_2}_2) + \frac{(1-\gamma)}{2} (m_1^{q_1} m'^{q_2}_2 + m_2^{q_1} m'^{q_2}_1 + m_1^{q_1} m'^{q_2}_1 + m_2^{q_1} m'^{q_2}_2) \right) \quad (3.22)$$

From (3.22), exact results of $\alpha_1(q_1,q_2)$, $\alpha_2(q_1,q_2)$ and $f(\alpha_1,\alpha_2)$ are obtained via (Appendix B).

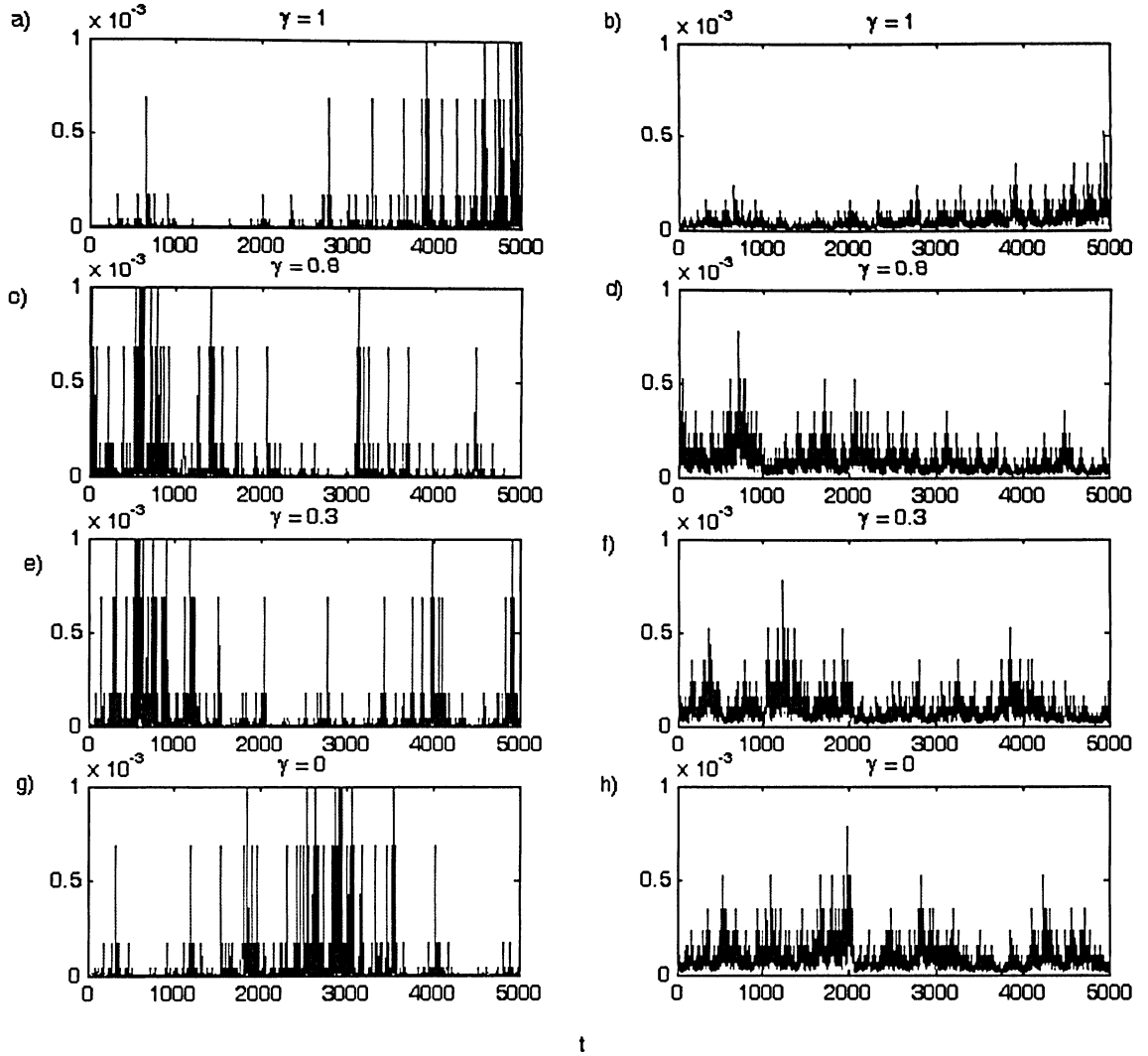

Figure 8 Studied binomial cascades. a) $\gamma = 1, m_1 = 0.2$ b) $\gamma = 1, m_1' = 0.4$ c) $\gamma = 0.8, m_1 = 0.2$ d) $\gamma = 0.8, m_1' = 0.4$ d) $\gamma = 0.3, m_1 = 0.2$ e) $\gamma = 0.3, m_1' = 0.4$ f) $\gamma = 0, m_1 = 0.2$ g) $\gamma = 0, m_1' = 0.4$. a), c), e), and g) correspond to $x_1(t)$ and b), d), f), and h) correspond to $x_2(t)$.

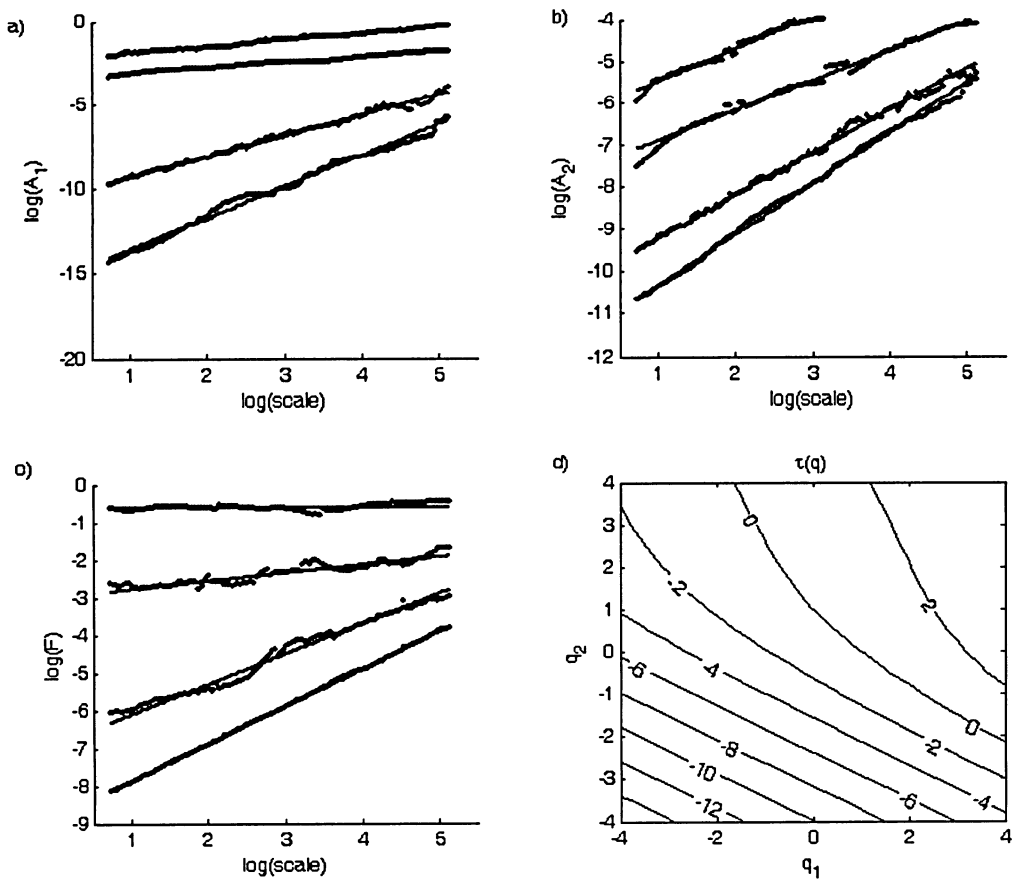

Figure 9 Canonical ensemble of partition function and τ obtained from the completely dependent binomial cascade.

Figs. 9a, b and c shows the typical results for the estimated A_1, A_2 and F. The thick lines are the estimated slopes. In Figs 9a and 9b, from top to bottom, $(q_1,q_2)=(3,-2),(4,0),(0,0),(-2,4)$. In Fig 9c, from top to bottom $(q_1,q_2)=(4,0),(3,-2),(-2,4),(0,0)$. Most remarkable is the predicted power law dependence in scale; see (3.14) and (3.15). This implies the validity of the scaling law $Z(a;q_1,q_2)\sim a^{\tau(q_1,q_2)}$ postulated in (3.4). From (3.14) and (3.15), the scaling exponents of these power law relationship yield the joint exponents, α_1, α_2 and the multifractal spectrum $f(\alpha_1,\alpha_2)$. The range of q_1, q_2 is limited to –4 to +4 with every increment of 0.5 in the numerical experiments. From α_1, α_2 and $f(\alpha_1,\alpha_2)$, the $\tau(q_1,q_2)$ is obtained according to (3.9). This is shown as a contour plot in Fig. 9d.

3.3.1 Completely Dependent Case

When $\gamma = 1$, the weight factors assigned to the two binomial cascades are completely dependent and results in a one-to-one relationship between the joint exponents: $\alpha' = \alpha'(\alpha)$. Furthermore, this implies $f(\alpha_1, \alpha_2)$ is a topological one dimensional curve in the $\alpha_1 - \alpha_2 - f$ space which is confirmed in Fig. 10a. In comparison with the theoretical prediction (B2), (B3), (B4), shown in (Fig. 10b), the numerical results are remarkably accurate. Comparisons with the individual multifractal spectra $f(\alpha_1)$ and $f(\alpha_2)$ can be conducted based on (3.18) and (3.19). In Fig. 10c, the crosses represent $\max_{\alpha_2} f(\alpha_1, \alpha_2)$ and the curve is the expected $f(\alpha_1)$. In Fig. 10d the crosses represent $\max_{\alpha_1} f(\alpha_1, \alpha_2)$ and the curve is the expected $f(\alpha_2)$. Again, they compare satisfactorily with the theoretical spectra. Deviation is seen to grow away from the maximum of the spectrum. This is mainly attributed to poor statistics as the regions correspond to large q_1, q_2 values.

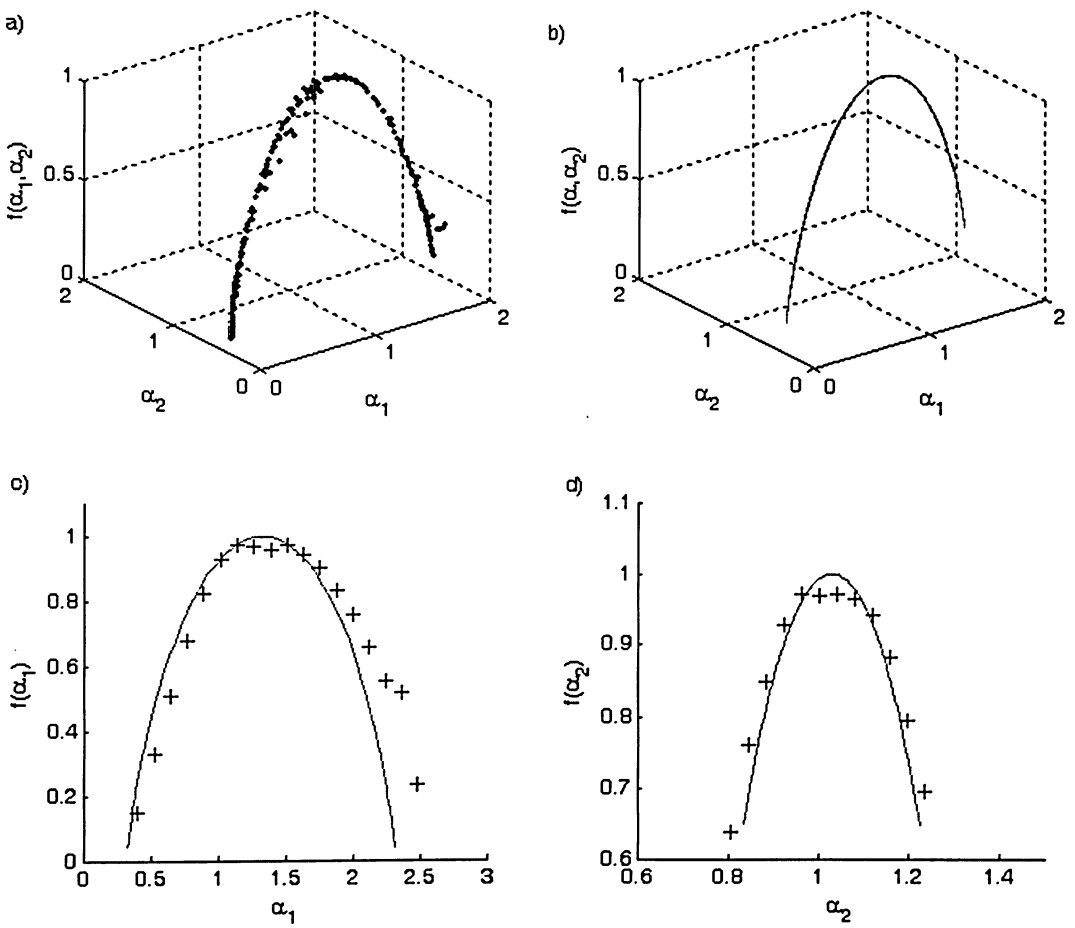

Figure 10 Completely dependent binomial cascades.

3.3.2 Partly Dependent Case

Partly dependent cascades are generated using $\gamma = 0.3$ and 0.8. When the weight factor assignment is not entirely dependent, a singularity in a certain part of $x_1(t)$ can be entirely independent of that of $x_2(t)$. As a result, a range of α_2 values are admissible for any given α_1 value. Hence, $f(\alpha_1, \alpha_2)$ is in general a 2D surface in the $\alpha_1 - \alpha_2 - f$ space. This characteristic is clearly captured in the joint analysis and depicted by contour lines (Figs. 11a and 11c). In addition, the details compare favorably with the theoretical predictions using (B2), (B3), (B4) shown in Figs. 11b and 11d. It should be noted that α_1, α_2 and f are derived as functions of q_1 and q_2. Figs. 11b and 11d are surface interpolations based on these functions and the discontinuous segments are attributed to a dearth of values in those regions. The more-elongated contour patterns of the $\gamma = 0.8$ case is evident and is a result of the stronger correlation of the weights of the cascades.

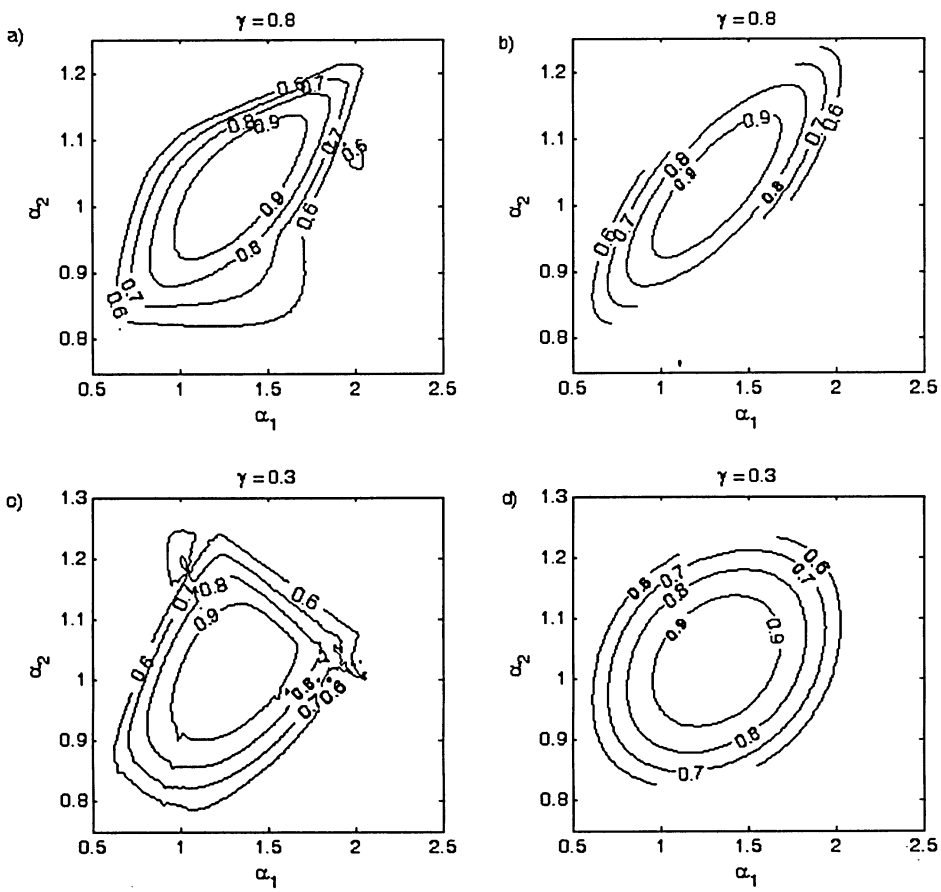

Figure 11 Contour plots for partly dependent binomial cascades

In Fig. 12, comparisons are made with the individual multifractal spectra $f(\alpha_1)$ and $f(\alpha_2)$. In Figs. 12a and 12c the crosses represent numerically obtained $\max_{\alpha_2} f(\alpha_1,\alpha_2)$ and the curves represent the expected $f(\alpha_1)$. In Figs. 12b and 12d the crosses represent numerically obtained $\max_{\alpha_1} f(\alpha_1,\alpha_2)$ and the curves represent the expected $f(\alpha_2)$. Again the numerically obtained results compare satisfactorily with the theoretical spectra.

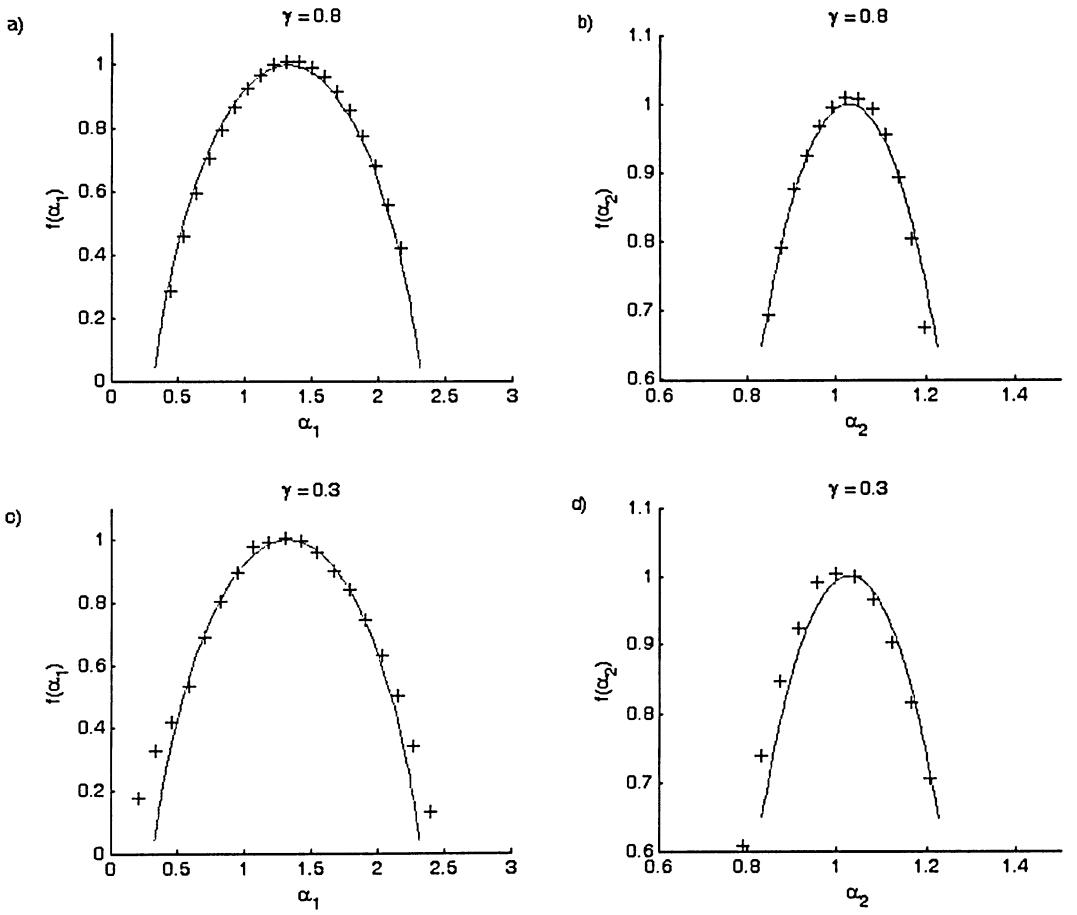

Figure 12 Validation of partly dependent binomial cascades.

3.3.3 Completely Independent Case

When $\gamma = 0$, the weights assigned to $x_1(t)$, $x_2(t)$ are completely independent to each other. This is manifested in the least elongated $f(\alpha_1, \alpha_2)$ in the $\alpha_1 - \alpha_2 - f$ space. This characteristic is also captured in the joint analysis (Fig. 13). Fig. 13a is the numerically obtained contour plot of $f(\alpha_1, \alpha_2)$ and Fig. 13b is the theoretically predicted contour plot. In Figs. 13c and 13d, the crosses represent $\max_{\alpha_2} f(\alpha_1, \alpha_2)$ and $\max_{\alpha_1} f(\alpha_1, \alpha_2)$ respectively, and the curves represent the expected $f(\alpha_1)$ and $f(\alpha_2)$ respectively.

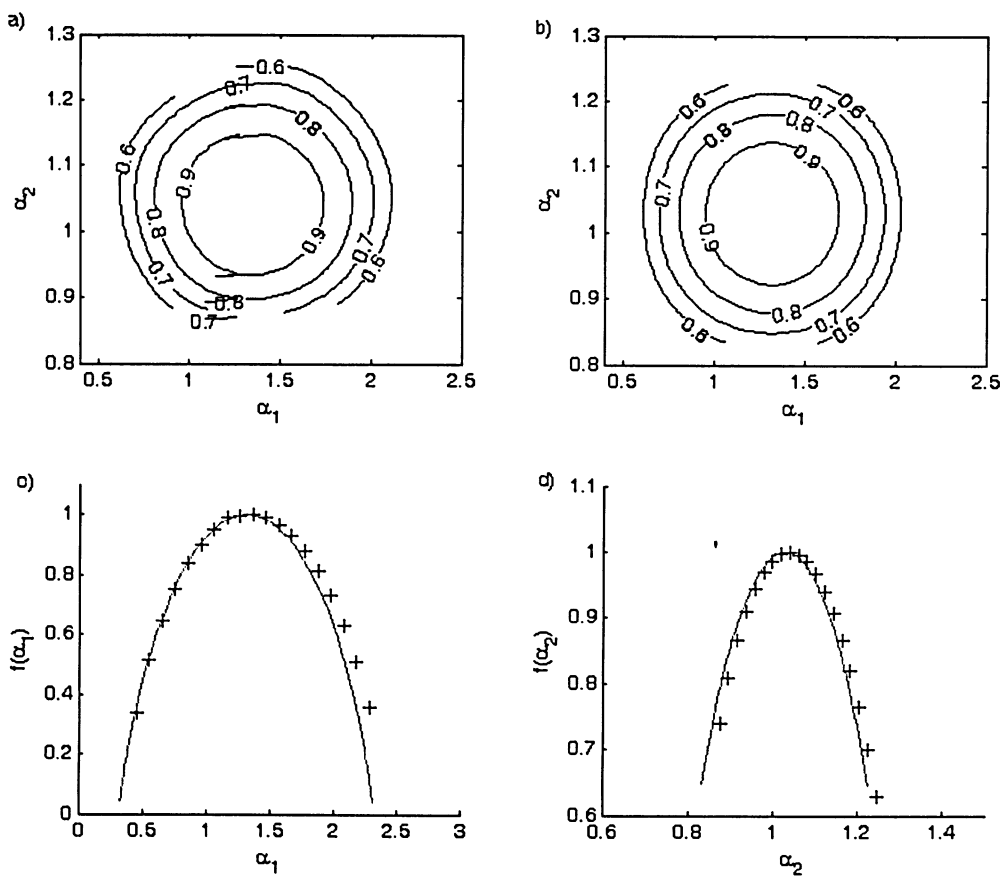

Figure 13 Completely independent binomial cascades.

CHAPTER 4 Joint WTMM Analysis of Physiological Signals of Healthy Humans

4.1 Introduction

The human body is without doubt one of the most complex dynamical systems in the physical world. For healthy humans, fractal characteristics were found in the fluctuation of almost all physiological data [21]. Thus, it is of great interest to examine the possibility of fractal correlation among any group of such simultaneously measured data sets. The goal of this chapter is to apply the joint WTMM analysis to heart rate and brain wave data from healthy young adults at rest. The motivation of choosing these two physiological data sets is to explore the potential origin of heart rate variability (HRV) of humans in the central nervous system (CNS).

The subject of HRV has been extensively studied in the past decade [22, 23, 24]. While there are strong peripheral influences on the beat-to-beat human heart rate, its origin remains largely unknown. From the nervous system point of view, it is known that the cardiovascular center in the medulla oblongata region is connected to the hypothalamus with further networking into the limbic system and the cortical structure of the brain [25]. It is therefore plausible that the central nervous system plays a part in HRV. The degree of such coupling that plays out in heart rate fluctuation is the subject that may be addressed by using the current approach.

Since a heartbeat is a field phenomenon carried out by millions of heart muscle cells, it is in principle not possible to define a unique instant for its completion. Fortunately, the majority of heart muscle cells carry out the necessary process associated with the heartbeat at roughly the same time. In practice, this is manifested in the sharp peak, known as the R-wave, in the electrocardiogram (ECG) measurement. As a result, HRV is typically characterized by the fluctuation of a beat-to-beat time interval between the R waves, known as the RR interval (RRi). This time interval measures, to a good approximation, the physiological events of the ventricular contraction.

Without invasive means, the cardiovascular center at the brainstem cannot be reached. But it is almost never explored due to its delicate structure and serious implication from any potential damage in the area. As an alternative, the surface scalp potential fluctuation of the brain was taken as the second signal to be used in the joint WTMM analysis. This is carried out by the standard procedure known as the electroencephalogram (EEG) [26]. For completeness, the backgrounds of EEG and ECG are given in section 4.2. The experimental setting is explained in section 4.3 and results are shown in section 4.4

4.2 Measuring Electrical Activities of the Brain and Heart

4.2.1 Surface Scalp Potential Measurement Based on Electroencephalogram

The smallest functional unit of the brain is the neuron. Movement of ions in and out of neuronal membrane produces electrical impulses and is the means of communication for neurons. Large numbers of neurons generating and conducting electrical impulses are responsible for the scalp potential fluctuation that is picked up by electrodes. In Fig. 14 the dark bar directly beneath the central electrode depicts a group of neurons which synchronously produce an impulse as depicted. However, the fluctuation picked up by the electrode itself is reduced in amplitude due to obstruction by the skull and scalp. If the cortical surface area involved in synchronous activity is small, the amplitude is reduced further as depicted by the electrode on the left. EEG recorded using electrodes is an average of cortical neuronal activity of small zones directly beneath the electrode [26].

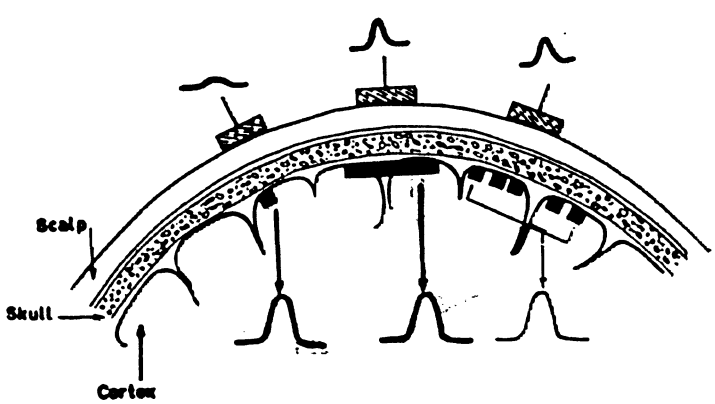

Figure 14 Electrodes placed on scalp. [26]

In this work, the bipolar method of EEG recording is used [27]. The idea is to place two electrodes at a certain given distance from the location of interest on the scalp and record the potential difference between them. Such readings are internally subtracted in the measuring device and the difference physically yields the electrical gradient along a straight line between the electrodes. Fig. 15 shows the schematics of such a setting. In Fig. 15, *e* represents the potential difference recorded by electrodes placed at A and B. As mentioned above, the skull and scalp are largely responsible for the resistance *r* inside the subject's head. Additional resistance R_1 and R_2 are encountered in the electrode-scalp interface which is bridged with highly conductive gel. An additional resistance R_{in} is found inside the amplifier. Surface scalp potential fluctuations are in the order of 10^{-6} V, and require amplification for data processing. Amplification puts limits on the amount of impedance between electrodes that can be tolerated without a significant loss of signal strength. Since the first EEG recordings by H. Berger, there have been great improvements in recording equipment, and modern amplifiers can tolerate an impedance of up to 50kΩ [27].

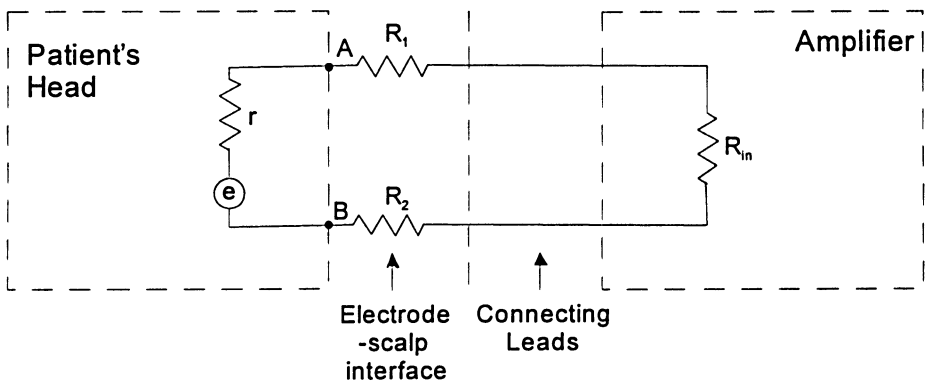

Figure 15 Simplified input circuit of EEG recording system. [26]

4.2.2 Heart Rate Monitoring Based on Electrocardiogram

The pattern of ECG depicts the physiological event of de-re-polarization of the heart muscle cells, starting from the sino-atrial (SA) node to atria, atrial-ventricular (AV) node, conduction fibers (His-Purkinje) and the ventricles. The schematic of the ECG of a heartbeat is shown in

Fig. 16. The de-re-polarization process manifests itself in characteristic spikes, known as the P, Q, R, S, T, waves in the ECG record, that signify the polarization sequence following roughly the order mentioned above [28]. Microscopically, such polarization is caused by the massive movements of ions in and out of the membrane of the heart muscle cells. The movements then result in a potential difference, which in turn can be picked up by the electrodes placed on the chest. The placement of the electrodes is generally arranged in a triangular shape known as Einthoven's triangle [29]. The heart rate $r(t)$ is taken as the time interval between successive R waves. The electrical recordings of the heart are much higher than EEG and are in the order of 10^{-3}V. It thus requires less amplification and the recording can tolerate higher impedance.

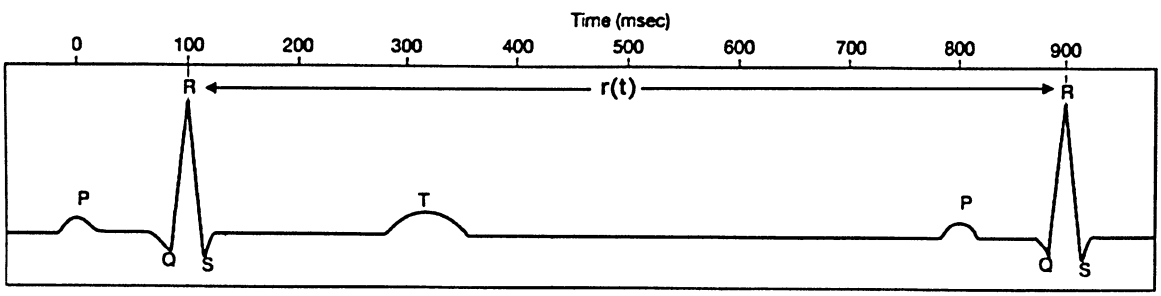

Figure 16 An ideal cardiac cycle from ECG.

4.3 *Experiments and EEG Data Post-Processing*

4.3.1 Experimental Protocol

Two subjects, all males, between the ages of 20-35 signed the consent form approved by the Ryerson University to participate in the experimental study. They were asked to maintain the normal sleeping and dietary routines and avoid vigorous exercise, alcohol and caffeine consumption during a two-day period before reporting to the recording session. There was no monetary compensation for their participation.

The simultaneous EEG and ECG recordings were completed in two stages. In the first stage, the subjects were asked to close their eyes and relax. The recording for this stage lasted for 15 minutes. In the next stage, subjects were asked to keep their eyes open, be relaxed, and were

given an art book [30] to arouse visual cortex activity. The recording for this stage lasted for 45 minutes. There was a brief break period between the two data recording stages. No specific time interval was designated for the break period. It is mainly for preparing the subjects to transit from the first to the second stage.

4.3.2 Instrumentation and Data Acquisition

Simultaneous recording of electrical activities of the heart and brain were conducted using the portable biosignal acquisition system (g.MoBIlab, Gtec Inc.) shown in Fig. 17a. The resolution of the Analogue-Digital Converter (ADC) was 16 bit, and the sampling frequency was 256Hz. The sensitivity range was 0-5V. Cleansing substance (isopropyl alcohol) was first applied to the scalp of the test subject before five surface scalp electrodes were positioned on specific locations of the scalp. The impedance was measured, and found to be less than 10kΩ in both subjects. The electrode placement, following the guidelines of the international 10-20 system [31], is shown in Fig. 17b. Specifically, they measure the neural network activities in left and right occipital areas, O1-C1, O2-C2, respectively. A ground electrode was connected to Fz. The gap between the electrode and scalp is filled with low-impedance material to facilitate conductivity (SIGNA Electrode Cream, Parker). The electrodes were first channeled to a pocket-size amplifier before they are displayed and saved on-line in a portable desktop assistant (Hewlett Packard iPAQ h5550). The schematic for the EEG acquisition is shown in Fig. 17b.

The g.MOBIlab portable device is capable of measuring the ECG activity as well. Towards that end, the European 5-lead ECG recording system was followed for the electrode placements on the chest. The potential difference picked up from the electrodes first passed through a 16-bit A/D conversion before it was digitally band-pass filtered in the range of 0.01-30 Hz. The signal was then passed onto the pocket-size amplifier and displayed and stored in the PDA. The schematic for the ECG acquisition is also shown in Fig. 17b.

a)

b)

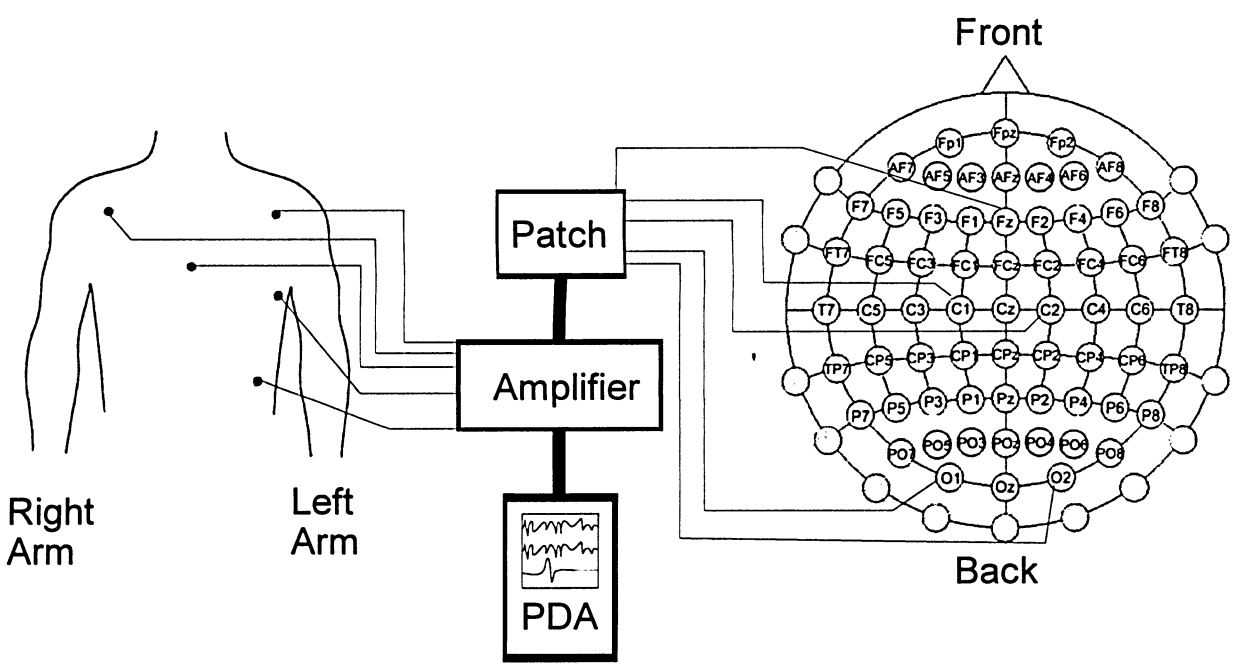

Figure 17 Experimental setup. a) Simplified schematic of experimental setup. B) g.MOBIlab system

4.3.3 EEG Data Post-Processing Using Heart Beat Interval Aggregation.

By embarking on the joint analysis of EEG and RRi, one must address the fundamental difference of the continuous-time EEG process and the discrete-time RRi process. Although the joint analysis is based on the maximum lines, the physiological meanings of EEG and RRi cannot be interpreted on a sample-to-sample basis. As a result, the EEG needs to be transformed or reduced on a beat-to-beat basis so as to 'compare' with the RRi. An effective way to achieve such data reduction is by the technique called aggregation [32].

Assume a continuous-time fractal process $x(t)$. The aggregated process is defined as

$$Y(t) = \sum_{t'=(t-1)d+1}^{td} x(t') \tag{4.1}$$

where d is called the aggregation parameter. If $x(t)$ is exactly self-similar, aggregation has no effect on the self-similar structure [32]. During the application of this technique to EEG, it is necessary to maintain a direct temporal relationship between EEG and RRi. Thus, the constant aggregation parameter d has to be replaced by the RRi. Let $E(t)$ and $r(t)$ be the measured EEG and RRi, respectively. Consider the modified aggregated EEG process

$$E_R(t) = \sum_{t'=(t-1)r(t)+1}^{r(t)t} E(t') \tag{4.2}$$

where $E_R(t)$ is the aggregated EEG.

Fig. 18 shows the effect of the aggregation (4.2) on the partition function. The EEG was aggregated using a constant aggregation parameter $d = 128$ and 64 and plotted along with the raw EEG ($E(t)$) and RRi aggregated EEG ($E_R(t)$). When the moments are close to 0 as in Figs. 18a, and 18b, the slope does not change significantly when compared to the non-aggregated. However, for large moments, such as $q = 2, -2$, there are differences in the slope as shown by Fig. 18c and d. Therefore, it is only practical to keep the moments low. In this work, the q range is set between -1 and +1.

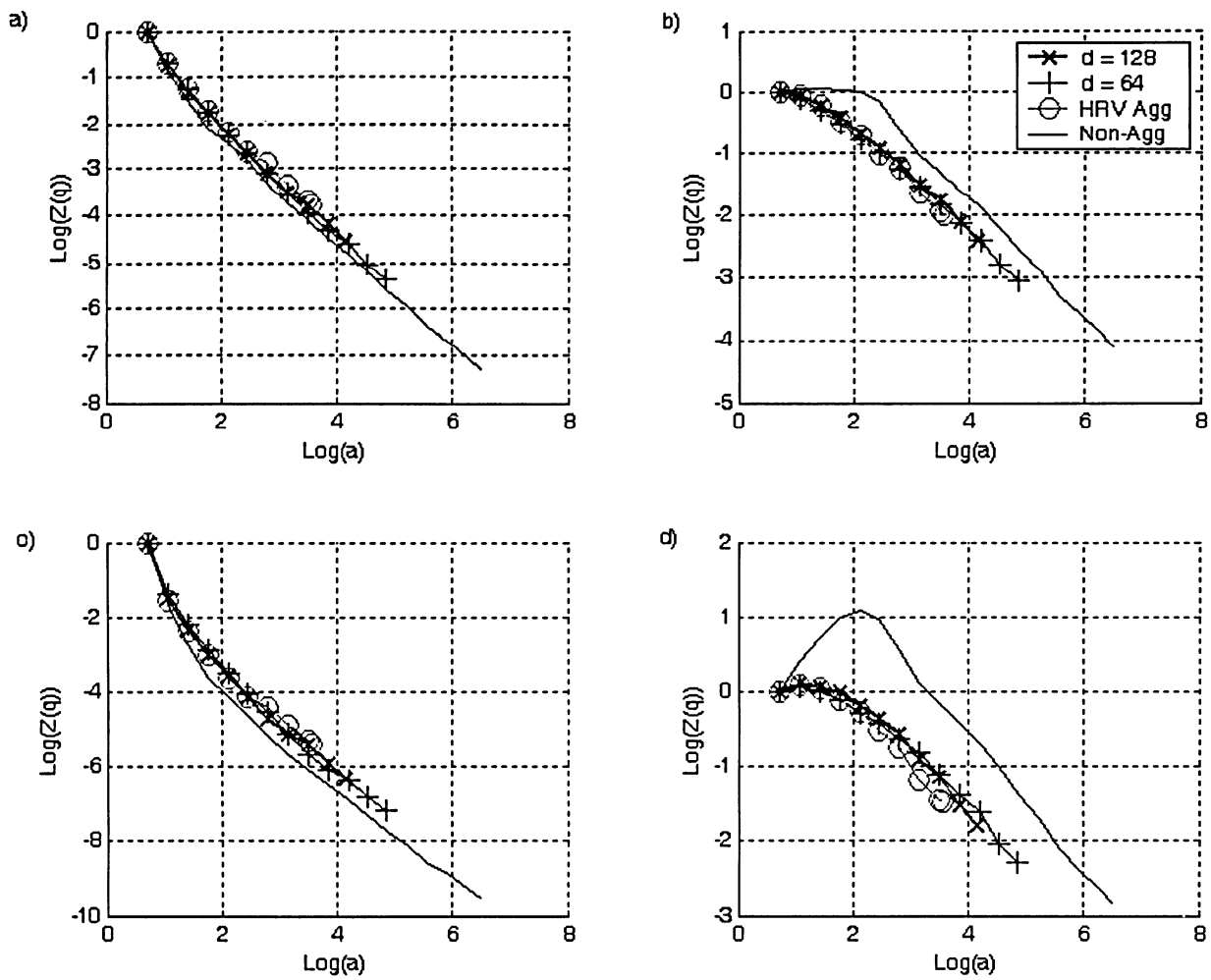

Figure 18 Comparison of Aggregated EEG from subject 1. a) q = -1, b) q = +1 c) q = -2, d) q = + 2.

4.4 Joint WTMM Analysis of Neural Activity of Occipital Cortex and Heart Rate Variability in Healthy Humans

4.4.1 General Characteristics of the Raw Data

The raw $E(t)$ and $r(t)$ are known to exhibit fractal characteristics [33, 23, 24]. Shown in Fig. 19 are the left, right EEG and $r(t)$ for the two subjects in eyes closed and open states.

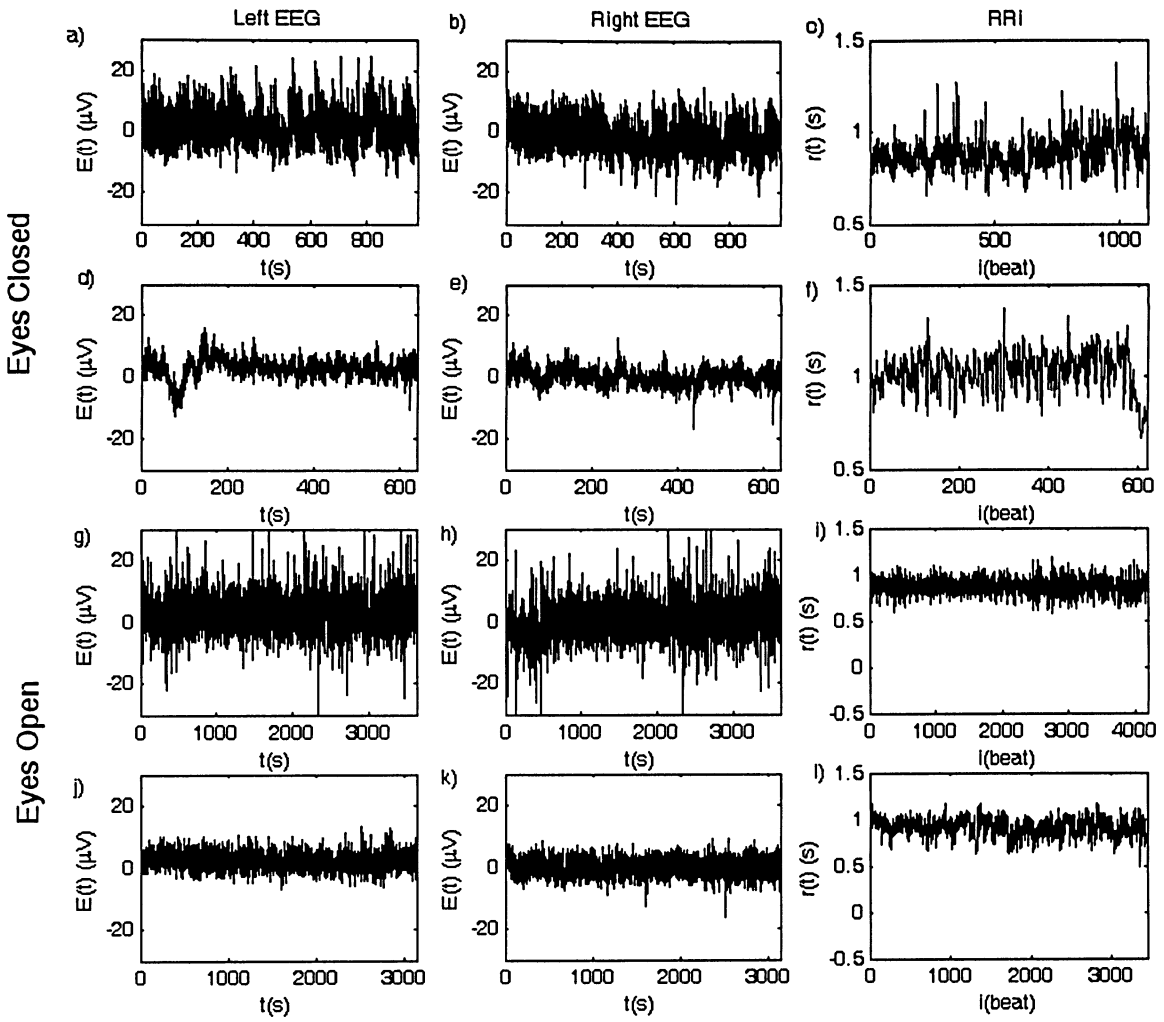

Figure 19 Raw EEG. a) Left EEG of subject 1 eyes closed. b) Right EEG of subject 1 eyes closed. c) RRi of subject 1 eyes closed. d) Left EEG of subject 2 eyes closed. e) Right EEG of subject 2 eyes closed. f) RRi of subject 2 eyes closed. g) Left EEG of subject 1 eyes open. h) Right EEG of subject 1 eyes open. i) RRi of subject 1 eyes open. j) Left EEG of subject 2 eyes open. k) Right EEG of subject 2 eyes open. l) RRi of subject 2 eyes open.

It is seen that the fluctuation pattern of the left, right EEG are qualitatively similar with more pronounced differences in the eyes closed than eyes open state (subject 2). In general, the difference between left and right EEG is known to be *not* significant due to the extensive neural pathways between the two hemispheres. At the present time, there is no satisfactory answer for the difference seen in subject 2. It is also evident that the EEG fluctuation is distinctively

different between the eyes closed and open states. This is expected as a 'resting' and active visual cortex involves very different neural circuitries in the brain, albeit the details of such difference remains open. From Fig. 19, it is seen that EEG fluctuation in the eyes open case covers a wider voltage range than in the eyes closed case.

The RRi was obtained from the R-wave interval of the ECG records. The difference between theeyes closed and open cases is seen to be qualitatively different. It is reasonable to suggest that the activity of the visual cortex (in eyes open) may be linked to the fluctuation manifested in HRV. As shown below, this correlation was indeed picked up in the joint WTMM analysis. In general, RRi records are seen to compose of 'patches' interrupted by intermittent downward spikes. The 'patch' region may be linked to the balance between the parasympathetic and sympathetic nervous system in the heart rate regulation. Occasional downward spikes are linked to instances of stronger sympathetic activities (faster heart rate). The extent of these heart rate increases is seen to be more evident during eyes open than in eyes closed. It is reasonable to imply that they characterize potential external stimuli exposed to the subject during eyes open. This is compatible to the qualitative difference of HRV discovered between sleep and wakefulness in healthy subjects [34].

4.4.2 Results from Joint WTMM Analysis.

Comparison of signals were made using all possible combinations within subjects. Both left and right EEG were compared between themselves and with HRV. The q range has been set to lie between -1 and $+1$ with a 0.1 increment. All results are presented based on the contour plot of $f(\alpha_1,\alpha_2)$ (Figs. 20 and 21).

For subject 1 in the eyes closed state (Fig. 20), the elongated contour line pattern compared with those of the artificial examples, such as Figs 10, 11, 13, suggests multifractal correlation between EEG and RRi and the left, right EEG. This is a surprising result as the cardiovascular center located at the brain stem is physically distant from the occipital area of the scalp. The detected correlation suggests potential interaction between the resting state of the visual cortex and the autonomic regulation of the heart rate.

In the eyes open state, the contour line pattern between left, right EEG and RRi is seen to become more 'circular,' suggesting a lesser degree of multifractal correlation between an active visual cortex and HRV. It is important to observe that the contour line pattern between the left, right EEG of this subject remains elongated in the eyes open state. This implies the correlation between left, right EEG remains intact even though there is a lack of correlation between EEG and HRV. This outcome is consistent with the fact that cardiovascular center and the occipital area of the scalp are separate.

The results for subject 2 are different from subject 1 in several aspects. While EEG and RRi multifractal correlation can be implied from the elongated contour line pattern, the comparison of Figs. 20a and 21a shows a different orientation: a negative correlation in both eyes closed and open states. Interestingly, in the eyes closed state, the contour line pattern of the right EEG and RRi is reversed from that of the left EEG and RRi (Figs 21a, 21c). This change in orientation is also manifested in the 'circular' contour line pattern between the left, right EEG themselves in the eyes closed state (Fig. 21e). The lesser degree of multifractal correlation in this case may suggest the lack of 'communication' between the left and right hemispheres of this subject in the eyes closed. The visible difference of the subject's left, right EEG records in the eyes closed state may be related to this outcome (Fig. 21). However, it is not possible to further explain the details at this time.

In the eyes open state, the reverse of the contour line pattern of EEG and RRi does not occur (Figs. 21b, 21d). This implies much better correlated left and right EEG activity. As a result, an elongated contour line pattern of the left, right EEG multifractal correlation (Fig. 21f) is seen.

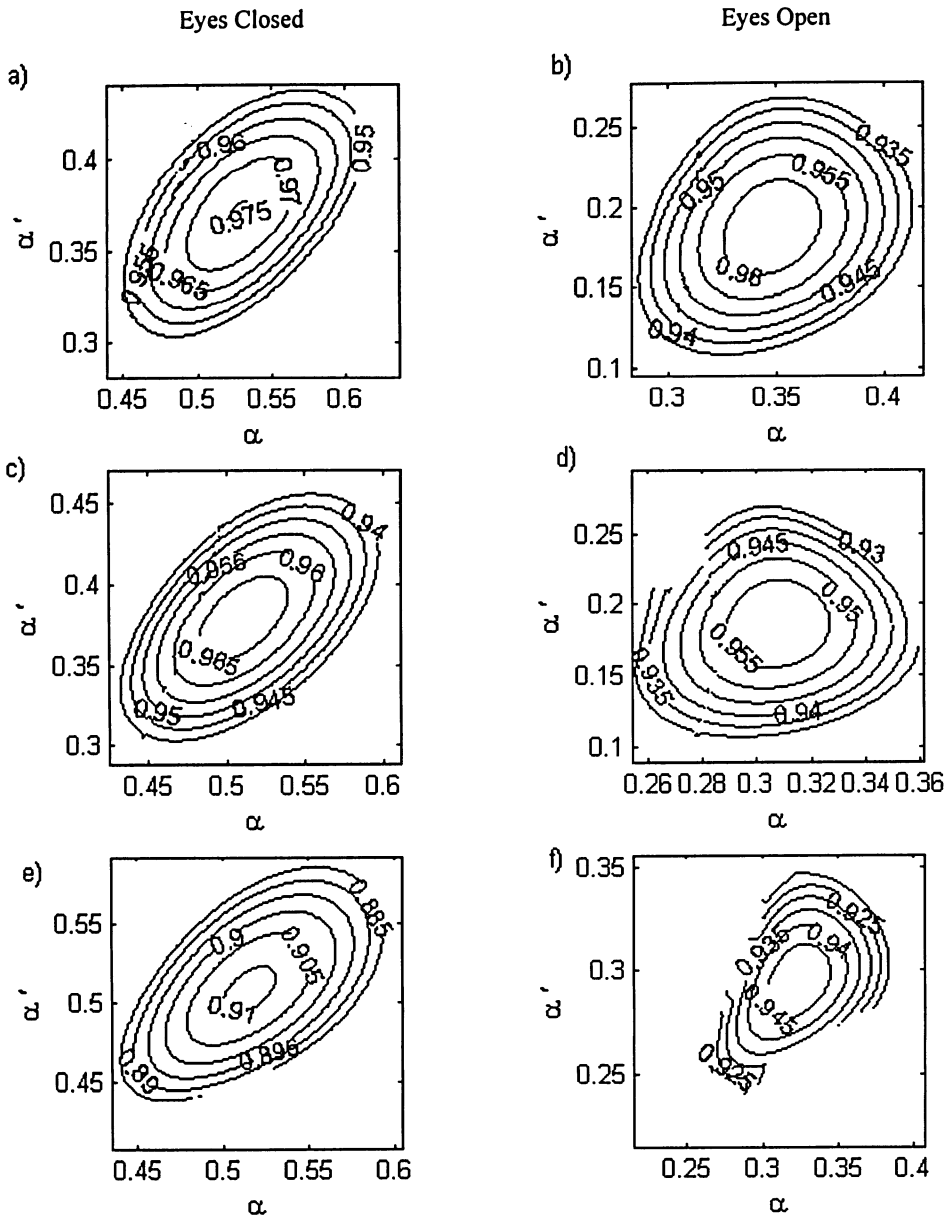

Figure 20 Contour plots of $f(\alpha_1, \alpha_2)$ for subject 1. a) and b) the left EEG is compared with HRV. c) and d) right EEG is compared with HRV. e) and f) left EEG is compared with right EEG.

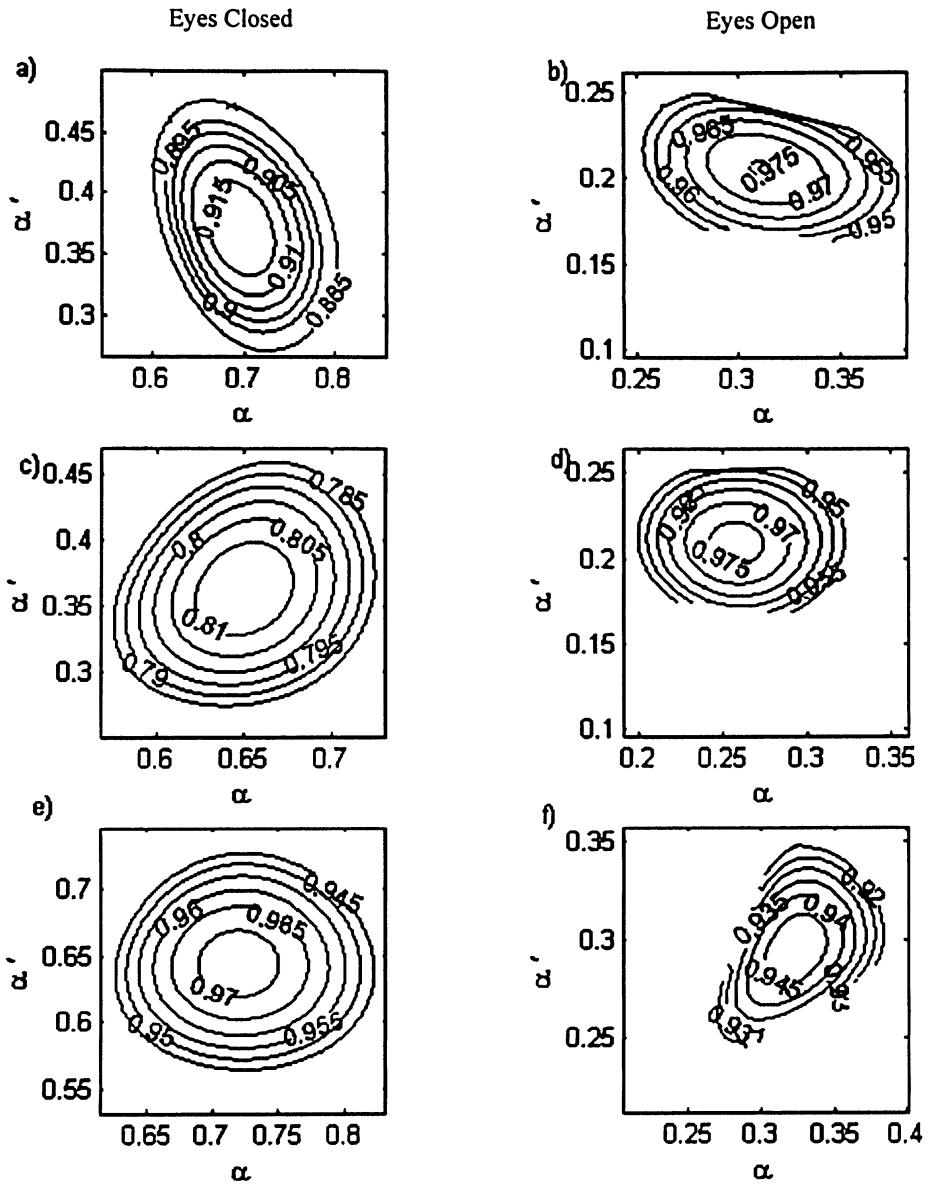

Figure 21 Contour plots of $f(\alpha_1, \alpha_2)$ for subject 2. a) and b) the left EEG is compared with HRV. c) and d) right EEG is compared with HRV. e) and f) left EEG is compared with right EEG.

CHAPTER 5 Discussion and Conclusion

In this work, the WTMM analysis of functions is extended from one time series to two time series, which is called the 2D WTMM analysis. As a result, one is able to compare the fluctuation patterns of simultaneously measured time series and begin to explore the subject of multifractal correlation. In this preliminary study, it was found that such a correlation can be readily observed by the elongation of contour lines of the joint $f(\alpha_1,\alpha_2)$. This feature is similar to the well known linear correlation analysis where strongly correlated random sequences are strongly oriented in the scatter plot of their individual realizations on a plane. In the present work, the interpretation of such a feature in 2D WTMM analysis is further supported by the theoretical prediction of the binomial cascades.

The 2D WTMM analysis also suffers from the same weaknesses prevalent in 1D WTMM. The heavy reliance of the algorithm on various slope estimations, such as (3.14) and (3.15), implies potential influence from human factors and the need to provide a more objective measure to gauge the quality of fit. The choice of the analyzing wavelet can also affect the result, although this is an 'inherent burden" of wavelet analysis in general.

Fundamentally, the extension to the 2D analysis is based on the assumption that the influence of singularities on the two time series is 'short term.' As a result, they contribute to maxima lines that are close to each other in the time-scale plane. This assumption can of course be relaxed. However, a more sophisticated 'pattern recognition' process appears necessary to achieve the goal of maxima lines pairing before 2D WTMM analysis can be invoked.

The 2D WTMM analysis is finally applied to simultaneously measured physiological time series taken from healthy human subjects. The availability of such a tool provides the potential to answer the open question of the origin of heart rate variability (HRV). While it is clear there is beat-to-beat modulation of the heart rate from the vascular and respiratory systems, it is believed that these components cannot fully explain the (massive) low-frequency signal power in heart rate and the general pattern of HRV. Over the years, a higher control center in the brain has been

suspected as the 'first contender' of the source of HRV. This study provides the first data testing of such a theory.

To perform the analysis, the idea of random aggregation based on the length of RRi (HRV aggregation) was used to 'discretize' the EEG. Within a small q range, aggregation was found to be capable of preserving the fractal property of EEG. Based on the orientation of the contour lines of $f(\alpha_1,\alpha_2)$, the preliminary data indicated that the fractal dynamics of HRV and EEG are indeed correlated, although there is no consistent type (positive or negative) or level of correlation. Such a linkage between EEG and HRV has not been demonstrated before and holds consequences for future analysis of physiological signals.

The range of α values are different between the eyes open and eyes closed state in both subjects. The maximum $f(\alpha_1,\alpha_2)$ value is located consistently at $\alpha > 0.5$ in the eyes closed state and $\alpha < 0.5$ in the eyes open state, which supports existing work [33]. It is inferred that a change in state affects the multifractal properties of EEG.

In diagnostic EEG, significant differences between hemispheres have been linked with disease [35]. It is thus initially expected that there will be a high level of correlation in the joint WTMM for left and right EEG for the healthy subjects who participated in this study. This feature was generally observed in the data except for subject 2 in the eyes closed state. With only one contradicting subject in the data pool, it is not possible to conclude with significance the general nature of this surprising find. If it is correct, it would suggest that a weaker hemispheric fractal correlation is possible in healthy persons and is more pronounced during the eyes closed state than the eyes open state. Such a disengagement between the hemispheric EEG fractal dynamics would inevitably link to the different functional networks that are invoked during the eyes closed and open states.

A foundation has been laid for further work into multifractal correlation using WTMM. It is necessary to form a quantitative assessment of the correlation and would be an appropriate

avenue for further development of the algorithm. In addition, the existing algorithm can also be extended to compare correlation between multiple time series.

APPENDICES

Appendix A Legendre Transform

Arnold's definition of the Legendre Transform is closely followed [36]. Let $f(x)$ be a convex function, $\frac{d^2 f}{dx^2} = 0$. The Legendre transform of the function f is a new function g of a new variable p. Let p be a given number. Consider the straight line $y = px$. $x(p)$ is defined at the point that is farthest away from the straight line in the vertical direction, i.e., for each p the function $px - f(x) = F(p,x)$ has a maximum with respect to x at the point $x(p)$ (see Fig. 22).

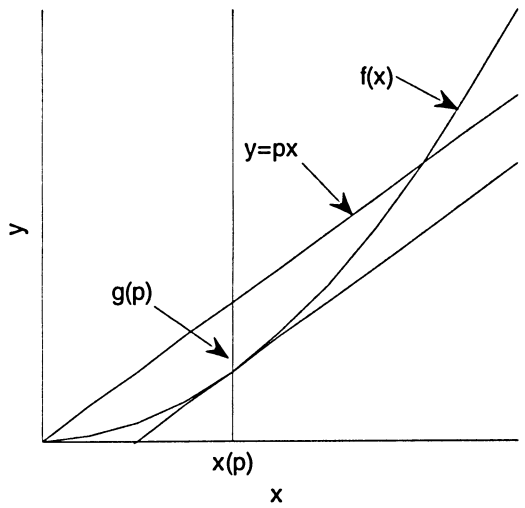

Figure 22 Legendre Transform

The Legendre transform is defined by $g(p) = F(p, x(px))$ where the point $x(p)$ is determined $\frac{\partial F}{\partial x} = 0$. A classical application of Legendre transform is the famous relationship between Lagrange and Hamiltonian formulation of mechanics. Given the Lagrangian $L(q,\dot{q},t)$ of the configuration variables q and its time derivative $\dot{q}$ of a dynamical system, the corresponding Hamiltonian is defined via the Legendre transform of L as a function of $\dot{q}$:

$H(p,q,t) = p\dot{q} - L(q,\dot{q},t)$, and the new variable $p = \frac{\partial L}{\partial \dot{q}}$ is the conjugate momentum.

Appendix B Exact results of $\alpha_1(q_1,q_2)$, $\alpha_2(q_1,q_2)$, and $f(\alpha_1,\alpha_2)$

Exact results of $\alpha_1(q_1,q_2)$, $\alpha_2(q_1,q_2)$ and $f(\alpha_1,\alpha_2)$ were obtained using Maple, where a1=m_1, a2=m_2, b1=m_1', b2=m_2', q=q_1, and p=q_2.

```
> tau:=-log(gamma*(a1^q*b1^p+a2^q*b2^p)+(1-
gamma)*(a1^q*b1^p+a1^q*b2^p+a2^q*b1^p+a2^q*b2^p)/2)/log(2);
```

$$t := -\frac{\ln\left(\gamma\,(a1^{q}\,b1^{p}+a2^{q}\,b2^{p})+\frac{1}{2}\,(1-\gamma)\,(a1^{q}\,b1^{p}+a1^{q}\,b2^{p}+a2^{q}\,b1^{p}+a2^{q}\,b2^{p})\right)}{\ln(2)} \tag{B1}$$

```
> alpha1:=simplify((diff(tau,q)));
```

$$a1 := -\frac{1}{\ln(2)\,(-\gamma a1^{q}\,b1^{p}-\gamma a2^{q}\,b2^{p}-a1^{q}\,b1^{p}-a1^{q}\,b2^{p}-a2^{q}\,b1^{p}-a2^{q}\,b2^{p}+\gamma a1^{q}\,b2^{p}+\gamma a2^{q}\,b1^{p})}\,($$

$$-\gamma a1^{q}\ln(a1)\,b1^{p}-\gamma a2^{q}\ln(a2)\,b2^{p}-a1^{q}\ln(a1)\,b1^{p}-a1^{q}\ln(a1)\,b2^{p}-a2^{q}\ln(a2)\,b1^{p}-a2^{q}\ln(a2)\,b2^{p} \tag{B2}$$

$$+\gamma a1^{q}\ln(a1)\,b2^{p}+\gamma a2^{q}\ln(a2)\,b1^{p})$$

```
> alpha2:=simplify(diff(tau,p));
```

$$a2 := \frac{1}{\ln(2)\,(-\gamma a1^{q}\,b1^{p}-\gamma a2^{q}\,b2^{p}-a1^{q}\,b1^{p}-a1^{q}\,b2^{p}-a2^{q}\,b1^{p}-a2^{q}\,b2^{p}+\gamma a1^{q}\,b2^{p}+\gamma a2^{q}\,b1^{p})}\,(\gamma$$

$$a1^{q}\,b1^{p}\ln(b1)+\gamma a2^{q}\,b2^{p}\ln(b2)+a1^{q}\,b1^{p}\ln(b1)+a1^{q}\,b2^{p}\ln(b2)+a2^{q}\,b1^{p}\ln(b1) \tag{B3}$$

$$+a2^{q}\,b2^{p}\ln(b2)-\gamma a1^{q}\,b2^{p}\ln(b2)-\gamma a2^{q}\,b1^{p}\ln(b1))$$

```
> f:=combine(alpha1*q+alpha2*p-tau);
```

$f :=$

$$-\frac{1}{\ln(2)\,(-\gamma a1^{q}\,b1^{p}-\gamma a2^{q}\,b2^{p}-a1^{q}\,b1^{p}-a1^{q}\,b2^{p}-a2^{q}\,b1^{p}-a2^{q}\,b2^{p}+\gamma a1^{q}\,b2^{p}+\gamma a2^{q}\,b1^{p})}\,((($$

$$-\gamma a1^{q}\ln(a1)\,b1^{p}-\gamma a2^{q}\ln(a2)\,b2^{p}-a1^{q}\ln(a1)\,b1^{p}-a1^{q}\ln(a1)\,b2^{p}-a2^{q}\ln(a2)\,b1^{p}-a2^{q}\ln(a2)\,b2^{p} \tag{B4}$$

$$+\gamma a1^{q}\ln(a1)\,b2^{p}+\gamma a2^{q}\ln(a2)\,b1^{p})\,q)+$$

$$\frac{1}{\ln(2)\,(-\gamma a1^{q}\,b1^{p}-\gamma a2^{q}\,b2^{p}-a1^{q}\,b1^{p}-a1^{q}\,b2^{p}-a2^{q}\,b1^{p}-a2^{q}\,b2^{p}+\gamma a1^{q}\,b2^{p}+\gamma a2^{q}\,b1^{p})}\,((\gamma$$

$$a1^{q}\,b1^{p}\ln(b1)+\gamma a2^{q}\,b2^{p}\ln(b2)+a1^{q}\,b1^{p}\ln(b1)+a1^{q}\,b2^{p}\ln(b2)+a2^{q}\,b1^{p}\ln(b1)$$

$$+ a2^{q}\, b2^{p} \ln(b2) - g a1^{q}\, b2^{p} \ln(b2) - g a2^{q}\, b1^{p} \ln(b1))\, p)$$

$$+ \frac{\ln\left(\left(g(a1^{q}\, b1^{p} + a2^{q}\, b2^{p}) + \left(\frac{1}{2} a1^{q}\, b1^{p} + \frac{1}{2} a1^{q}\, b2^{p} + \frac{1}{2} a2^{q}\, b1^{p} + \frac{1}{2} a2^{q}\, b2^{p}\right)(1-g)\right)\right)}{\ln(2)}$$

Appendix C Canonical Ensemble Formulation of Partition Function

Equation (3.14) and (3.15) are results from elementary calculus. Consider $k = 1$. By (3.4) and (3.9), one has

$$\frac{\partial Z}{\partial q_1}(a;\mathbf{q}) \sim a^{r(q)} \log(a) \frac{\partial \tau}{\partial q_1} = a^{r(q)} \log(a) \alpha_1 . \tag{B5}$$

The average (3.11) can now be written as

$$\sum_j \nu \log\left(\left|\overline{W}_{i,j}\right|\right) = \frac{\partial Z / \partial q_1}{Z} . \tag{B6}$$

Equation (3.14) follows after substituting (B5) in (B6). Notice the problematic prefactor in (3.4) is cancelled out in (B6). For $k = 2$, the derivation is the same.

Based on (B6), the average (3.13) can be written as

$$\sum \nu \log(\nu) = q_1 \frac{\partial Z / \partial q_1}{Z} + q_2 \frac{\partial Z / \partial q_2}{Z} - \log(Z) . \tag{B7}$$

Again, using (B5), (3.15) results after substituting (3.9).

REFERENCES

[1] L. Nottale, *Fractals and the quantum theory of spacetime.* International Journal of Modern Physics A, **4**, 5047-5117, 1989.

[2] R. N. Mantegna and H. E. Stanley, *Stock market dynamics and turbulence: parallel analysis of fluctuation phenomena.* Physica A, **239**, 255-266, 1997.

[3] W. E. Leland, M. Taqqu, W. Willinger, and D. Wilson, *On the self-similar nature of ethernet traffic (Extended Version).* IEEE/ACM Transactions on Networking, **2**, 1-15, 1994.

[4] A. Arneodo, B. Audit, E. Bacry, S. Manneville, J. F. Muzy, and S. G. Roux, *Thermodynamics of fractal signals based on wavelet analysis: application to fully developed turbulence data and DNA sequences.* Physica A, **254**, 24-25, 1998.

[5] B. Mandelbrot, *Fractal geometry of nature.* W. H. Freeman. New York, 1983.

[6] A. B. Chhabra, C. Meneveau, R. V. Jensen, and K. R. Sreenivasan, *Direct dertermination of the $f(\alpha)$ singularity spectrum and its application to fully developed turbulence.* Physical Review A, **40**, 5284-5294, 1989.

[7] W. Hwang and S. Mallat, *Characterization of self-similar multifractals with wavelet maxima.* Applied and Computational Harmonic Analysis, **1**, 316-328, 1994.

[8] E. Bacry, J. F. Muzy, and A. Arneodo, *Singularity spectrum of fractal signals from wavelet analysis: exact Results.* Journal of Statistical Physics, **70**, 637-673, 1990.

[9] P. C. Ivanov, M. G. Rosenblum, C. K. Peng, J. Mietus, S. Havlin, H. E. Stanley, and A. L. Goldberger, *Scaling behaviour of heartbeat intervals obtained by wavelet-based time-series analysis.* Nature **383**, 323-327, 1996.

[10] H. Peitgen, H. Jürgens, and D. Saupe, *Chaos and fractals : new frontiers of science.* Springer-Verlag. New York, 1992.

[11] D. Sornette, *Discrete-scale invariance and complex dimensions.* Physics Reports, **297**, 239-270, 1998.

[12] I. Daubechies, *Ten lectures on wavelets.* SIAM. Philadelphia,1992.

[13] C.L. Tien, J.H. Lienhard, *Statistical thermodynamics.* Hemisphere Publishing Corporation. New York, 1985.

[14] T. C. Halsey, M. H. Jensen, L. P. Kadanoff, I. Procaccia, and B. Shraiman, *Fractal measures and their singularities: the characterization of strange sets.* Physical Review E, **33**, 1141-1151, 1986.

[15] B. Mandelbrot and J. Ness, *Fractional brownian motions, fractional noises and applications.* SIAM Review, **10**, 422-437, 1968.

[16] J. L'evy-Vehel, *FracLab: a fractal analysis toolbox for signal and image processing.* http://fractales.inria.fr/, 2006.

[17]K. Sreenivasan and C. Meneveau, *The fractal facets of turbulence.* Journal of Fluid Mechanics, **173**, 429-484, 1986.

[18] C. Meneveau, K. R. Sreenivasan, P. Kailasnath, and M. S. Fan, *Joint multifractal measures: theory and applications to turbulence.* Physical Review A, **41**, 894-913, 1990.

[19] L. A. Smith, J. D. Fournier, and E. A. Spiegel. *Lacunarity and intermittency in fluid turbulence.* Physics Letters A, **114A**, 465-468, 1986.

[20] A. Chhabra, C. Meneveau, R. Jensen, and K. Sreenivasan, *Direct determination of the $f(\alpha)$ spectrum and its application to fully developed turbulence.* Physical Review A, **40**, 5284-5294, 1989.

[21] J. Bassingthwaighte, *Fractal physiology.* Oxford University Press. New York, 1994.

[22] Task Force of the ESC and NASPE, *Heart rate variability.* European Heart Journal, **17**, 354-381 1996.

[23] P. Ivanov, L. Nunes Amaral, A. Goldberger, S. Havlin, M. Rosenblum, Z. Struzik, and E. Stanley, *Multifractality in human heartbeat dynamics.* Letters to Nature, **399**, 461-465 1999.

[24] D. C. Lin and R. L. Hughson, *Modelling heart rate variability in healthy humans.* Physical Review Letters, **86**, 1650-1653, 2001.

[25] C. O. Trouth, R. M. Millis, H. F. Kiwull-Schöne and M. E. Schläfke, *Ventral brainstem mechanisms and control of respiration and blood pressure.* Marcel Dekker. New York, 1995.

[26] R. Cooper, J. W. Osselton, and J. C. Shaw, *EEG technology.* Butterworths. London, 1974.

[27] P. Nunez and R. Srinivasan, *Electric fields of the brain: the neurophysics of EEG.* Oxford University Press. New York, 2006.

[28] J.R. Levick, *An introduction to cardiovascular physiology.* Butterworth & Co Publ. New York, 1991.

[29] E. Nash and V. Nahas, *Understanding the ECG.* Chapman & Hall. Melbourne, 1995.

[30] H. W. Janson and A. F. Janson, *History of art.* Prentice-Hall. New York, 2001.

[31] H. Jasper, *The ten-twenty electrode system of the international federation.* EEG Clinical Neurophysiology, **10a**, 731-735, 1958.

[32] K. Kant, *On Aggregate Traffic generation with Multifractal Properties.* Proceedings of GLOBECOM 2000. Rio de Janeiro, 2000.

[33] D. C. Lin, A. Sharif, and H. Kwan, *Scaling and organization of electroencephalographic background activity and alpha rhythm in healthy young adults.* Biological Cybernetics. http://dx.doi.org/10.1007/s00422-006-0094-4, 2006.

[34] F. Jurysta, P. van de Borne, P. Migeotte, M. Dumont, J. Lanquart, J. Deagaute, P. Linkowski, *A study of dynamic interactions between sleep EEG and heart rate variability in healthy young men.* Clinical Neurophysiology, **114**, 2146-2155, 2003.

[35] E. Basar, *EEG-Brain Dynamics: relation between EEG and brain evoked potentials.* Elsevier/North Holland. Amsterdam, 1980.

[36] V. I. Arnold, *Mathematical methods of classical mechanics, 2 ed.* Springer-Verlag. New York, 1989.